Computational Studies of Small Molecule Activation in Catalysis and Green Chemistry

A Thesis Presented for the

Bachelor of Science in Chemistry, American Chemical Society

Certified, Honors Concentration

Degree

The University of Tennessee, Knoxville

Alexa Griffith

May 2019

Dedication

In loving memory of my grandaddy, Charles N. Griffith. For always being my biggest supporter and encouraging me to follow my dreams.

Acknowledgments

I would like to thank my family and friends, especially my mom, for putting up with me through college.

I would also like to thank the University of Tennessee, the Department of Chemistry, and the research advisors I have had the honor of working under, Dr. Konstantinos Vogiatzis and Dr. Michael Best. To Justin Kirkland, Dr. Charles Feigerle, Dr. Jeffrey Kovac, Jeff Elliot, and Jacob Townsend, I greatly appreciate your support and guidance.

Abstract

Recently, society has relied on scientists for creating cleaner and more sustainable chemical processes, giving rise to research efforts in the field of "Green Chemistry." This trend is predicted to grow in the coming years and is aimed at generating low waste, efficient, healthy, and safe scientific procedures. Biocatalysis plays an important role in the field of Green Chemistry due to the biodegradability and mild reaction conditions characteristic of biological catalysts. Biomimetic studies show promise for clean energy solutions through the imitation of the structure and function of an enzyme active sites.[1]

The Vogiatzis group at the University of Tennessee focuses its research on describing chemical systems relevant to Green Chemistry. Through electronic structure theory methods, our goal is elucidate the electronic structure of small molecules containing transition metals and gain insight on their available catalytic mechanisms.

The role of transition metal-mediated oxidation of alkanes has proven to be one of the greater challenges in various branches of chemistry.[2] Consequently, the elucidation of the mechanistic aspects that lead to the catalytic conversion of methane to methanol has received considerable attention. Small molecules containing iron(IV)-oxo have been observed to functionalize the C-H bond of methane in mononuclear heme and non-heme enzymes. The process converting methane to methanol is currently used for industrial applications, and an effort to understand the ligand environment that leads to the C-H bond functionalization is of high interest.[3]

Nitrogen, essential to all living organisms, is found abundantly in our atmosphere in its unusable form, dinitrogen. Nitrogen "fixation" describes a process that converts N_2 into a usable, nitrogen-containing molecule. The well known industrial Haber-Bosh process was a revolutionary discovery that paved the way for large production of fertilizers that aid

the growth of crops. Although the Haber-Bosch process has many benefits to society, the environmentally hazardous process is heterogeneously catalyzed by hydrogen gas and iron. The heat and fossil fuel material required for the reaction imposes concerns about health, sustainability, and efficiency. Biomimetic studies have focused solutions around a class of enzymes known as nitrogenases. Molybdenum nitrogenase enzymes are able to perform efficacious nitrogen fixation under ambient conditions. For this reason, our group aims to elucidate the electronic structure of dinitrogen-molybdenum moieties and gain a better understanding of the binding activity between molybdenum and dinitrogen.

Table of Contents

1 Theoretical Background **1**

1.1 Computational Chemistry 1

1.2 Hartree-Fock Theory 3

1.3 Density Functional Theory 5

1.4 Functionals 7

1.5 Basis Sets 8

1.6 Multireference Methods 11

2 Computational Studies of Molybdenum Dinitrogen Binding Activity **14**

2.1 Introduction 14

2.2 Methods 21

2.3 Results and Discussion 23

2.4 Conclusions 28

3 Computational Studies on the Electronic Structure of Iron(IV)-Oxo Transition States **30**

3.1 Introduction 30

3.2 Computational Details 37

3.3 Results and Discussion 40

3.4 Conclusion 45

3.5 Concluding Remarks 47

Bibliography **48**

List of Tables

2.1 MoN_2 PES Data 24

2.2 $[MoN_2]^{2+}$ PES Data 26

2.3 $[MoN_2]^{3+}$ PES Data 28

3.1 Unconstrained TS model results for $[FeO(NH_3)_4]^{2+}$ 41

3.2 Unconstrained TS model results for $[FeO(NH_3)_4]^{2+}$ 41

3.3 Optimized Geometry Analysis of $[FeO(NH_3)_4]^{2+}$ 42

3.4 Constrained TS model results for $[FeO(NH_3)_4]^{2+}$, π-channel 44

3.5 Constrained TS model results for $[FeO(NH_3)_4]^{2+}$, σ-channel 45

List of Figures

1.1 Slater- versus Gaussian-type function 9
1.2 Comparison of CGTO's with an STO using the STO-nG Pople basis set . . . 10
1.3 Illustration of CASSCF subspaces 12

2.1 Molybdenum nitrogenase. (A) MoFe protein complex with the Fe protein homodimer on the left half of the protein, and the right side depicts the MoFe protein α subunit in green, and the β subunit in cyan. (B) Models of the three different metal clusters: the 4Fe4S cluster (F), P-cluster (P), and FeMo-co (M).[4] 16
2.2 (a) Reaction scheme of the Haber-Bosch process (b) Reaction scheme of the FeMo cofactor active site in nitrogenase[5] 17
2.3 Synthesized molybdenum based complexes: (a) & (b) PPP-pincer catalysts by Nishibayashi (c) Mo-complex that cleaves the N_2 triple bond by Cummins (d) Schrock mononuclear Mo-catalyst[6] 18
2.4 Two proposed cycles for the catalytic formation of ammonia 19
2.5 Proposed molybdenum-nitrogen based systems 20
2.6 Diatomic ligand binding modes[7] 21
2.7 Illustration of the 12 molecular orbitals in the active space of this study . . . 22
2.8 Potential energy surfaces of MoN_2 with a color map indicating the range of height (CASPT2 energy) of the surface 24
2.9 Potential energy surfaces of $[MoN_2]^{2+}$ with a color map indicating the range of height (CASPT2 energy) of the surface 26
2.10 Potential energy surfaces of $[MoN_2]^{3+}$ with a color map indicating the range of height (CASPT2 energy) of the surface 27

3.1 Lunsford catalytic scheme[8] . . . 31
3.2 Hydroxylation scheme with a high-valent iron-oxo intermediate[9] . . . 32
3.3 Synthesized iron(IV)-oxo complexes[10] . . . 32
3.4 Iron-oxo porphyrin complex study by Nam, where Ar is a functional ligand[11] 33
3.5 Valence molecular orbital diagram of FeO^{2+}[3] . . . 34
3.6 Four possible σ and π channels of Fe(IV)-oxo with (a) near-trigonal pyramidal field of an S = 2 species and (b) near-tetragonal field of an S = 1 species[3] . . 35
3.7 (a) Orbital overlap predictions of $^3TS_\pi$ and $^5TS_\sigma$ and (b) hydrogen abstraction TS geometries[12] . . . 36
3.8 Model complex used in this work: $[FeO(NH_3)_4]^{2+}$, near-C_{3v}, (Fe: orange, N: blue, O: red, H: white) . . . 37
3.9 $[FeO(NH_3)_4]^{2+}$ + CH_4 TS σ- and π- channel angles (Fe: orange, N: blue, O: red, H: white, C: grey) . . . 40
3.10 $[FeO(NH_3)_4]^{2+}$ molecular orbital diagram . . . 42
3.11 Molecular orbital diagrams of the σ- and π-TS species . . . 43

Chapter 1

Theoretical Background

1.1 Computational Chemistry

The main goal of electronic structure theory methods is better understand the nature of matter by solving the electronic Schrödinger equation for a given n-electron system. A key assumption allowing for the development of computational methods is the Born-Oppenheimer Approximation, which states that the nuclei can be approximated as fixed points in space due to the large size difference between the electron and nucleus. Since nuclei are much heavier than electrons, they move significantly slower. This allows for the kinetic energy term of the nuclei to be disregarded and the repulsive term of the nuclei to be set constant.[13] The separation of nuclear and electronic motion allows for a good approximation of the Schrödinger equation

$$\hat{H}\psi = E\psi \tag{1.1}$$

The left side of the Schrödinger equation is composed of a Hamiltonian operator and a wave function, and the right side is given by a scalar, E, corresponding to the total energy of the system, and the same wavefunction. The wave function ψ is an eigenfunction with respect to the Hamiltonian, and E represents its eigenvalue. The Hamiltonian operator can be written in terms of the kinetic ($\hat{T}$) and potential energy ($\hat{V}$)

$$\hat{H} = \hat{T} + \hat{V} \tag{1.2}$$

When substituting the kinetic and potential energy terms into the Schrödinger equation and rewriting the kinetic term, we get

$$\left(-\frac{\hbar}{2\mu}\nabla^2 + V(\mathbf{r}) \right)\psi = E\psi \tag{1.3}$$

for the hydrogen atom where μ represents the reduced mass of the system, and the Laplace operator, ∇^2, is given as the divergence of the gradient of a function on Euclidean space. The potential energy term V($\mathbf{r}$) is also known as the Coulomb interaction. The Coulomb interaction is the attractive potential responsible for holding the electron and nucleus together and depends on the distance, $\mathbf{r}$. The potential energy term V($\mathbf{r}$) can be written as

$$V(\mathbf{r}) = \frac{-Ze^2}{4\pi\epsilon_0 \boldsymbol{r}} \tag{1.4}$$

Z represents the nuclear charge (Z=1 for hydrogen), e is the charge of an electron, the constant ϵ_0 is the permittivity of vacuum, and the interaction between the nuclei and electron is dependent upon the distance, $\mathbf{r}$. The definition of the Coulombic and kinetic terms give the hydrogen Hamiltonian as

$$\hat{H} = -\frac{\hbar}{2\mu}\nabla^2 - \frac{Ze^2}{4\pi\epsilon_0 \mathbf{r}} \tag{1.5}$$

The Schrödinger equation for a hydrogen atom can be separated into radial and spherical parts. The spherical harmonic functions result in the commonly recognized orbital shapes, and the radial function represents the term containing the distance between the nucleus and the electron. Approximating and optimizing the radial component of the Schrödinger equation is a large focus in computational chemistry and will be discussed in the following section on basis sets.[14]

Once a multielectron system is introduced, approximations are needed to solve the Schrödinger equation. For example, the Schrödinger equation for a two-body system such as the He atom is written as

$$-\hbar^2\left[\frac{1}{2\mu}\left(\nabla_1^2+\nabla_2^2\right)\right]\psi(\boldsymbol{r_1},\boldsymbol{r_2})+\frac{e^2}{4\pi\epsilon_0}\left[\frac{1}{\boldsymbol{r_{12}}}-Z\left(\frac{1}{\boldsymbol{r_1}}+\frac{1}{\boldsymbol{r_2}}\right)\right]\psi(\boldsymbol{r_1},\boldsymbol{r_2})=E\psi(\boldsymbol{r_1},\boldsymbol{r_2}) \quad (1.6)$$

The electron-nucleus distance vectors are denoted as r_1 and r_2, respectively. The distance between the two electrons is given as r_{12}. Similar to the hydrogen equation, the kinetic energy term is defined with the Laplace operators, one for each electron, and the attractive potential is given by the terms in the Hamiltonian containing $\frac{1}{r_1}$ and $\frac{1}{r_2}$. The computational difficulty arises from the repulsive potential between the two electrons, and is represented by the Hamiltonian term containing a dependence on the distance between the two electrons, r_{12}. The repulsive potential term requires approximations since the variables in the term are not separable, and therefore, we cannot solve it directly. The Hamiltonian for an n-body problem quickly becomes increasingly complex due to the inability to separate variables in the repulsive potential term.[13] Electronic structure theory methods are needed for solving complex n-body problems where good approximations essential to obtaining relevant results.

1.2 Hartree-Fock Theory

Single determinant Hartree-Fock (HF) theory, also known as Self-Consistent Field (SCF) theory, aims to solve the Schrödinger equation for a set of spin orbitals that form a single determinant. (1.7)

$$|\psi_0\rangle = |ab\cdot\cdot\cdot\cdot\cdot n\rangle \quad (1.7)$$

Given an electronic Hamiltonian, the aim of HF theory is to get a good approximation of the ground state energy of an N-electron system. The spin orbitals can be changed in order to reach the minimal energy, which is accomplished through the variational method, as long as they meet the condition of being orthonormal. (1.8)

$$\langle a|b\rangle = \delta_{ab} \quad (1.8)$$

where δ_{ab} is the Kronecker delta. When the energy is at the minimum, the corresponding spin orbitals are regarded as the optimal set of spin orbitals for the system.[13]

The Fock operator ($\hat{f}$) is used as the Hamiltonian in the HF method. The HF equation is a pseudo-eignenvalue equation that uses spin orbitals as eigenfunctions and the resulting eigenvalues as orbital energies.

$$\hat{f}|a\rangle = \epsilon_a|a\rangle \tag{1.9}$$

The orbital energies as expectation values of the Fock operator

$$\epsilon_a = \langle a|\hat{f}|a\rangle \tag{1.10}$$

The sum of the one electron orbital energies alone is not the total energy of the ground state of the system. The total energy includes both exchange and coulomb terms resulting from the interactions between two electrons. The sum of the two electron integrals is doubly accounted for, and for this reason, equation (1.11) includes a factor of one-half

$$E_0 = \sum_a^N \langle a|\hat{f}|a\rangle + \frac{1}{2}\sum_a^N \sum_b^N \langle ab||ab\rangle \tag{1.11}$$

The first term on the right-hand side of the equation is the sum of the one-electron integrals, while the second contains the sum of all the two-electron integrals from the exchange and coulomb terms.

HF makes approximations based on the assumption that one determinant is a sufficient description of a wave function, which is not always the case, and the SCF method assumes that electrons can be described in terms of a mean-field where an electron interact with an average charge distribution. The Coulomb integral used in HF replaces the electron-electron repulsion term in the Schrödinger equation with an integral containing the charge densities of two electrons and solves for the average repulsion. This induces an error into the HF energy known as the correlation energy

$$E_{corr} = E_{exact} - E_{HF} \tag{1.12}$$

The HF method assumes that two electrons with the same spin have a zero probability of occupying the same point in space, but predicts a nonzero probability for electrons with different spins. Therefore, electrons with different spins are uncorrelated in HF, but electrons with the same spin are considered correlated.

Restricted HF (RHF) is a common form of HF which implies that each of the spatial molecular orbitals is doubly occupied. Unrestricted HF (UHF) is another HF method used when there are unpaired electrons in a system. This allows for different spatial orbitals based on electron spin. RHF typically gives a bad description of molecules at long bond lengths where dissociation occurs. For example, RHF fails to accurately depict H_2 as it dissociates and the hydrogens behave as an open shelled system. On the other hand, the RHF gives a better description than UHF at equilibrium.

The RHF equation can be solved by using the Roothaan equations. The Roothaan equations convert the differential equation to a set of algebraic equations using matrix techniques by introducing a basis set. The overlap and Fock matrices are formed by substituting the basis linear expansion into the HF equation, affording the Roothaan equations

$$\mathbf{FC} = \mathbf{SC}\epsilon \tag{1.13}$$

1.3 Density Functional Theory

As discussed in the first section, the time-independent, nonrelativistic Shrödinger equation (1.1) is an eigenvalue equation composed of a wavefunction ψ that is an eigenfunction of the Hamiltonian operator $\hat{H}$ that results in the same wavefunction ψ and the energy eigenvalue, E. In most cases, the more complicated Schrödinger equation concerning electrons interacting with multiple nuclei is needed. Density functional theory (DFT) provides another method for solving the many-body problem.[15]

A measurable quantity is the probability that N electrons are at a given set of coordinates ($\mathbf{r}_1$, $\mathbf{r}_2$,..,$\mathbf{r}_n$). The probability is measured by the wave function with respect to $\mathbf{r}_n$ multiplied by its complex conjugate. Due to not differentiating between electron one, two, etc., the

interest lies in the probability that the set of electrons have the coordinates $\mathbf{r}_1$, $\mathbf{r}_2$,..,$\mathbf{r}_n$. The density of electrons at a given position in space is expressed in the equation below

$$n(\mathbf{r}) = 2\sum_i \psi_i^*(\mathbf{r})\psi_i(\mathbf{r}) \tag{1.14}$$

The summation of the electron wave functions gives the probability that a wave function $\psi(\mathbf{r})$ is located at position $\mathbf{r}$. Physically observable information can be derived from the Equation 1.14. The multiplication by a factor of two arises from the ability of the orbitals to hold two electrons, one spin up and the other spin down.[15]

Kohn and Hohenberg provided two fundamental theorems for density functional theory (DFT) known as the Hohenberg-Kohn theorems. One theorem states that "the full many-particle ground state is a unique functional of n($\mathbf{r}$)."[16] Therefore, this theorem proves that when solving the Schrödinger equation for the ground-state energy, the electron density is unique to that functional and establishes a direct correlation between ground-state energies and their electron densities.[15] The second theorem relates the minimal energy of the system and its corresponding electron density as the true electron density for the full solution of the Schrödinger equation.

Using the following equation, Kohn-Sham equations solve for the electron density by considering single-electron wave functions

$$\left[(\frac{-\hbar^2}{2m})\ \nabla^2 + V(\mathbf{r}) + V_H(\mathbf{r}) + V_{XC}(\mathbf{r})\right]\ \psi_i(\mathbf{r})\ =\ E_i\psi_i(\mathbf{r}) \tag{1.15}$$

and contains the summation of three potentials. V($\mathbf{r}$) describes the potential between the electron and the atomic nuclei. The V_{XC} term represents the exchange-correlation and is not exactly known. To solve for this, functionals with approximations are used. The V_H term corresponds to the Hartree potential. This term describes the Coulomb repulsion of an electron with the whole electron density.[15]

To solve for the ground-state energy using the DFT method, a trial electron density is chosen to start with. This first guess is calculated by solving the Kohn-Sham equation. (2.1) Using the resulting wave functions, the next step is to calculate the electron density using

Equation (1.14). If these match, the solution has been found. If not, a new trial function is chosen.[15]

1.4 Functionals

The exchange-correlation functional used in DFT calculations is an approximation. The local density approximation (LDA) was developed to better describe the exchange-correlation contribution. The LDA functional is given by

$$E_{XC}^{LDA}[n(\mathbf{r})] = \int n(r)\varepsilon_{XC}(n(r))dr \tag{1.16}$$

The ε_{XC} term represents the known exchange-correlation energy for each particle in a uniform electron gas with density n. For systems with varying density, corrections have been developed. The LDA allows for the Kohn-Sham equation to be solved, but does not solve the Schrödinger equation exactly.[17]

Another approximation that is better suited for smaller systems, the generalized gradient approximation (GGA), relies on information about the electron density's local gradient. The local gradient takes into account that electron densities are not typically uniform but vary spatially. Many different GGA functionals have been developed and are commonly used today.[15]

There are two main categories of functionals: empirical and nonemperical. Made to employ when using experimental data or *ab initio*, respectively, empirical functionals are parametrized to fit experimental data. Nonemperical functionals have more criteria to satisfy and are used to solve the Kohn-Sham equatons given a certain set of constraints. A higher degree of accuracy is achieved when more constraints are met in a given GGA nonemperical functional.[15]

Some of the most popular functionals are a subset of GGA functionals known as hybrid functionals. Hybrid functionals contain components from both the exact exchange and the GGA functional. For example, the B3LYP functional is a popular hybrid functional due to closely correlating with experimental results.[18] These types of functionals do not satisfy the

uniform density limit, which is why they are useful for smaller molecules where the electron density is more varied than in bulkier systems.[15]

1.5 Basis Sets

Basis sets are used for constructing an appropriate wave function in quantum chemistry. Mathematically, basis sets are defined as a set of vectors that span a space in which a problem is solved. For application in quantum chemistry, a basis set gives the wave function a vector representation. For the purpose of building a wave function, a basis set is a set of non-orthogonal, one particle functions. Basis functions are used to build molecular orbitals and are expanded as linear combinations with coefficients. Typically, basis functions are centered on atoms but it is possible to have basis functions centered on bonds. For the purposes of this study, the basis sets centered on atoms will be considered. Often referred to as the LCAO-MO (linear combination of atom orbitals) approximation, the molecular orbitals are built from a linear combination of atomic orbitals[13]

$$\psi(\boldsymbol{r}) = \sum_i c_i x_i(\boldsymbol{r}) \tag{1.17}$$

Molecular wave functions formed from a set of basis functions have both a radial and spherical component, and the description of the radial part is the essential component of the basis function. The radial component is commonly represented by Slater-type and Gaussian-type orbitals (STOs and GTOs). The Slater-type orbital is of the form $e^{-a\mathbf{r}}$ where a is a constant known as the Slater exponent and controls the width of the orbital, and the Gaussian-type orbital is of the form $e^{-a\mathbf{r}^2}$ where a controls the width of the orbital. The dependency on the distance of the electron from the atomic nucleus, $\mathbf{r}$, is the key difference between Slater-type and Gaussian-type orbitals. The major behavioral differences in the two functions occurs when the distance, $\mathbf{r}$, is equal to zero or large. The cusp is incorrectly described when $\mathbf{r}$ is zero, and the exponential tail incorrectly describes the decay rate when $\mathbf{r}$ is large. The Slater-type function has a finite slope whereas the Gaussian-type function has a slope of zero.

In the simplest example, a hydrogen atom, the Slater-type orbital gives an accurate depiction of the 1s atomic hydrogen. The normalized 1s Slater-type function (1.18) more accurately describes the 1s hydrogen atomic orbital than does the normalized 1s Gaussian-type function (1.19).

$$\psi_{1s}(a, \mathbf{r\text{-}R}) = (\frac{a^3}{\pi})^{\frac{1}{2}} e^{-a|\mathbf{r\text{-}R}|} \tag{1.18}$$

$$\psi_{1s}(a, \mathbf{r\text{-}R}) = (\frac{2a}{\pi})^{\frac{3}{4}} e^{-a|\mathbf{r\text{-}R}|^2} \tag{1.19}$$

The generalized equation of Slater- and Gaussian-type orbitals are defined below in Equation 1.20 and 1.21, respectively. The variable a represents the orbital exponent.

$$\psi_{STO} = (\frac{2a}{\pi})^{1/2} e^{-a\boldsymbol{r}} \tag{1.20}$$

$$\psi_{GTO} = (\frac{a^3}{\pi})^{3/4} e^{-a\boldsymbol{r}^2} \tag{1.21}$$

As the number of orbitals begin to grow, computing the Slater-type functions becomes increasingly difficult. The accurate description of the 1s atomic hydrogen's electron density near the nucleus is best shown by the kusp of the Slater-type function. Figure 1.1 illustrates the differences in the general Slater- and Gaussian-type functions

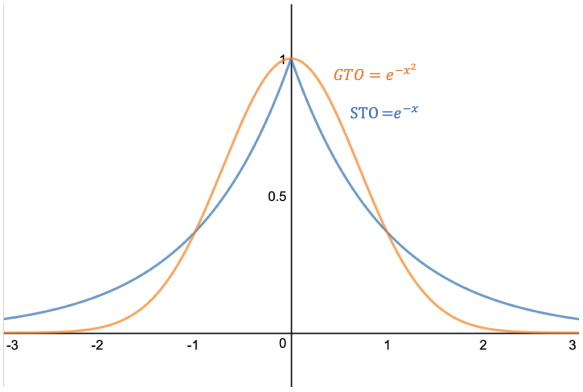


Figure 1.1: Slater- versus Gaussian-type function

The electron density near the nucleus forms a cusps, as proved in Kato's cusp condition, also known as Kato's theorem.[19] This is computationally demanding to solve, therefore, GTOs provide a feasible approximation.

Due to the computational difficulties accompanied with the Slater-type function, the solution is to use Gaussian-type orbitals (GTOs) as a linear combination, which are known as contracted Gaussian-type orbitals (CGTOs). For molecular calculations, Gaussian primitives make up CGTOs. Linear combinations of primitives are used as basis functions with fixed coefficients and exponents.[20] Below is the generalized equation for a CGTO basis function where N is equal to the normalization constant

$$\psi_{CGTO} = \sum_{i=1}^{n} c_i N e^{-a_i \boldsymbol{r^2}} \tag{1.22}$$

The more primitives in the basis set, the better the approximation the CGTOs are to the STOs, as shown in Figure 1.2

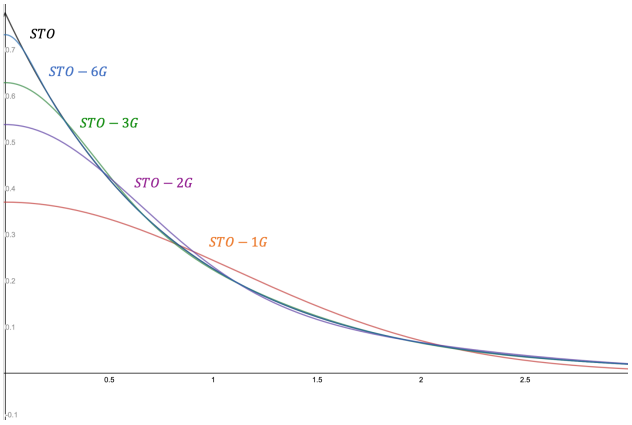


Figure 1.2: Comparison of CGTO's with an STO using the STO-nG Pople basis set

Basis sets expand upon CGTOs to describe the physical behavior of molecular orbitals. A minimal basis is defined as having one basis function per atomic orbital in the atom (CGTO, GTO, or STO). Using CGTOs, a basis set can contain any number of primitive functions, but this does not always capture the flexibility of molecular orbitals. Extended basis sets use multiple functions to describe each atomic orbital, expanding the basis function and more accurately describing molecular orbital flexibility. Extended basis sets are typically denoted by zeta (ζ). The double- and triple-ζ basis sets are frequently employed and correspond to a

basis set that has two or three basis functions per atomic orbital, respectively. Although one can keep extending the basis, the addition of basis functions is computationally expensive and other solutions are available.

Two types of additional extensions of basis sets are useful in this paper's studies. Often it is not necessary to have an extended set of basis functions for core atomic orbitals, and to compensate for this, split valence basis sets are implemented. A split valence basis sets assigns one basis function for each core atomic orbital and a given number of contracted basis functions to each valence atomic orbital. Furthermore, polarization functions are useful for describing the flexibility of the orbital as another atom approaches it. As an atom gets closer to another, the orbitals may prefer to shift to one side. This shifting is best simulated by mixing the basis functions of an orbital with angular momentum ℓ with basis functions of ℓ + 1.

1.6 Multireference Methods

In some cases, a single determinant is not sufficient description of the electronic structure where near degenerate electronic states exist, such as transition metals and when describing the breaking or forming of a bond. RHF and UHF methods (described in the HF section) each have their disadvantages. RHF does not correctly describe dissociation, and UHF is not an eigenfunction of the spin operator. At least two determinants are required to preserve a spin eigenfunction. An approach known as multiconfigurational self-consistent field (MCSCF) is used for this purpose.

The MCSCF wave function depends on both a parameter associated with the orbitals and a parameter related to the configuration interaction (CI) vectors and can be written as

$$|\psi_0(\mathbf{k},\mathbf{c})\rangle = e^{-\hat{k}} \sum_m c_m |\psi_m\rangle \tag{1.23}$$

where the spin orbitals undergo unitary transformation by exponential term with the operator k, and c_m represents the CI-vector expansion coefficients. The MCSCF wave function is

contrived by variationally optimizing the configuration interaction (CI) coefficients (c) and the molecular orbital (MO) coefficients (k)

$$E_{MCSCF} = \underset{k,c}{min} \frac{\langle \psi_0(\mathbf{k},\mathbf{c})|\hat{H}|\psi_0(k,c)\rangle}{\langle \psi_0(\mathbf{k},\mathbf{c})|\psi_0(\mathbf{k},\mathbf{c})\rangle} \tag{1.24}$$

The complete active space self-consistent-field (CASSCF) method is an extension of HF that differentiates between three subspaces: inactive, active, and virtual orbitals. The active space, or the full configuration interaction (FCI) space, includes every possible electronic configurations in a given system constrained to a particular spin and spatial symmetry. In CASSCF, the FCI is reduced to include only the configuration functions (CFs) that represent doubly occupied orbitals in the inactive space and empty orbitals in the virtual space. Therefore, the FCI expansion is only found in the active space. The active space is either determined by prior knowledge of the chemical problem (for example, which orbitals are involved in bond breaking or forming of the system) or must be experimented with. An illustration of the CASSCF subspaces is given in Figure 1.3.[21]

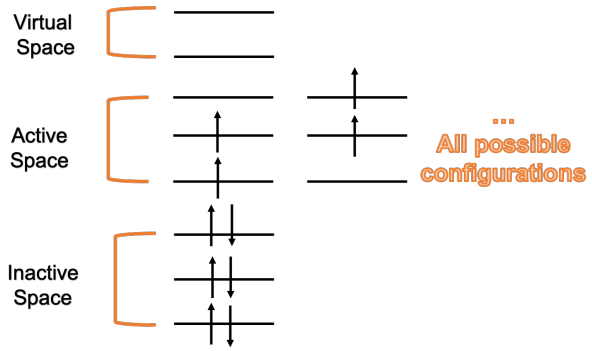


Figure 1.3: Illustration of CASSCF subspaces

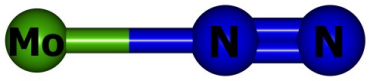
The CASSCF method describes static correlation effects due to considering multiple configurations in the active space but is missing dynamic correlation, which is associated with the instantaneous correlation among the electrons due to their mutual repulsion.[22] CASPT2 methods provide dynamic correlation by expanding the CI coefficients on the MR wave function. The CASPT2 method is typically applied to the CASSCF wave function to include dynamic correlation effects and this method is denoted as CASSCF/CASPT2.

The combined CASSCF/CASPT2 methods are useful for a variety of quantum chemical problems. Applications such as the study of the electronic structure and spectroscopy of a

transition metal complexes, spin-orbit coupling in actinide chemistry, photochemistry, and much more.[21]

Chapter 2

Computational Studies of Molybdenum Dinitrogen Binding Activity



2.1 Introduction

Comprising of more than 78% of our atmosphere, nitrogen, in its dinitrogen (N_2) form, is one of the most abundant gases on Earth.[23] Additionally, nitrogen is one of the most important elements for life, essential for survival and growth in all living systems. Dinitrogen itself is unusable, and it is necessary to convert N_2 into a usable form (a nitrogen containing species) or "fixing" nitrogen.[24] Organisms capable of fixing and growing on N_2 as the sole nitrogen source are known as diazotrophs and typically complete this process under ambient conditions.[25] Studies have used biological inspiration as the basis for many nitrogen fixation studies in an attempt to mimic the biological process and create an environmentally friendly synthetic route.[6;26;27;28;29;30] A man-made, sustainable nitrogen fixation process for the application of promoting crop growth is of extreme importance to our world today due to society's enormous, and growing, food consumption.[31]

The most common forms of utilizable nitrogen are NO_3^- and NH_4^+, which are commonly employed in fertilizers. These compounds are highly valuable for bolstering crop growth due to nitrogen depletion severely limiting the growth of plants and crops.[32] NH_4^+ binds with negatively charged ions in soil and is then available for absorption by the plant. Although the uptake of ammonium from fertilizers is advantageous for the growth of crops, there are some disadvantages associated with the efficiency of fertilizers. Nitrifying and denitrifying bacteria in the soil compete for both NO_3^- and NH_4^+ respectively, exploiting the compounds for energy.[33] Nitrifying bacteria discharge nitrate, while denitrifying bacteria expel N_2 back into the atmosphere. Washing away into ground water is another unintended fate for NO_3^-. Overall, both of these alternate paths for of fertilizer make up two-thirds of the material used. Only about one-third of the amount of fertilizer used succeeds in facilitating growth in crops and plants. Therefore, approximately only one-third of the energy used for creating fertilizer is efficiently used.[25]

Nitrogen fixation can occur via oxidation or reduction. Some natural, oxidative processes include lightning and combustion, which account for nearly 10% of fixed nitrogen. Reductive, man-made processes account for nearly 30%; biological reduction processes account for nearly 60% and occur at ambient temperature and pressure, without the use of H_2. In biological processes, usable nitrogen is vital for many prokaryotes (archea and bacteria), which are microscopic organisms adroit in perform nitrogen fixation.[25] One example is nitrogenase enzymes that are commonly found in bacteria and play a vital role in the fixation of N_2. Nitrogenases perform the reduction of N_2 to ammonia via the mechanism below[34]

$$8e^- + 8H^+ + N_2 \rightarrow 2NH_3 + H_2 \tag{2.1}$$

Scientific studies began over 150 years ago when Jodin suggested that microbes were capable of N_2 fixation.[35] The name "nitrogenase" was coined in 1934 by a scientist named Burk who conducted the first significant studies in living cells.[36;37] Beginning in the 1960's, scientists had developed mechanisms for extracting active nitrogenase, allowing mechanistic investigations to begin.[38;39;40] The decades that followed saw many advancements in the structural and mechanistic characterization of nitrogenase.[41;42;43]

A report by Burgess and Lowe published in 1996 summarized many key discoveries made in the past 35 years.[44] For instance, nitrogenase was determined to be composed of two parts, one component was the MoFe protein dinitrogenase, and the other was dinitrogenase reductase, the electron-transfer Fe component.[43;45;46;47;48;49;50] A second discovery revealed that the catalysis required a reducing source, MgATP. Third was the revelation that single electron transfer and MgATP hydrolysis cause the nitrogenase and dinitrogenase components to associate and dissociate in the catalytic cycle.[47] Another key discovery described the composition of the MoFe protein. Two metal clusters, the P-cluster and the iron-molybdenum cofactor (FeMo-co) reside in the MoFe protein. Substrate binding and reduction occurs at the MoFe-co active site, and the main role of the P-cluster is electron transfer between the Fe protein to the FeMo protein.[41;51;48;52;53;54;55;42;53;56;57;58] (Figure 2.1) Finally, another important discovery during this time period was the various types of nitrogenases besides molybdenum. The molybdenum in FeMo-co is interchanged with vanadium and iron in V- and Fe-type nitrogenases.[59] Although substantial progress was made during this time, the details of the catalytic mechanism remained unexplained.

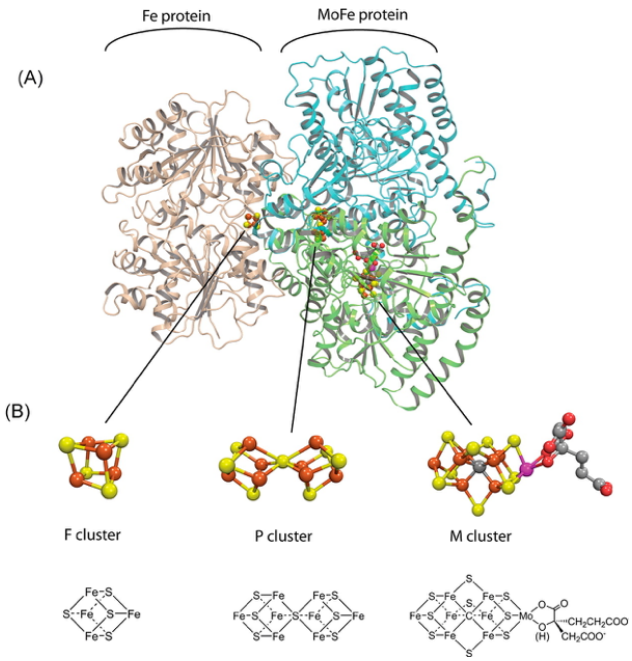


Figure 2.1: Molybdenum nitrogenase. (A) MoFe protein complex with the Fe protein homodimer on the left half of the protein, and the right side depicts the MoFe protein α subunit in green, and the β subunit in cyan. (B) Models of the three different metal clusters: the 4Fe4S cluster (F), P-cluster (P), and FeMo-co (M).[4]

These early advances paved the way for great developments in the understanding of the structural and functional components of nitrogenase. Mechanistic proposals based on the identity of the interstitial atom in the MoFe cofactor were controversial due to a previous assumptions (for example, studies were conducted assuming nitrogen was the interstitial atom) made from an inability to identify the atom with certainty.[60;61;62] The interstitial atom is an important aspect of the MoFe-co due to its speculative role in breaking the N_2 triple

bond. Recently, high resolution X-ray diffraction studies have aided in clearly identifying the interstitial atom located in the MoFe cofactor.[63] The clarification of the interstitial atom in the FeMo-co puts scientists one step closer to understanding the perplexing nature of the active site. In addition to spectroscopic studies, computational studies have assisted in elucidating the FeMo-co structure and mechanism.[26;27;28;29;64;65;66;67;68;69;70] For example, computational studies by Siegbahn concurred with the X-ray structures suggesting that the interstitial atom of the MoFe cofactor was carbon.[71] Studies are still needed to clarify the specific structural role of the carbon in the center of the MoFe cofactor. Other studies leading to advancements in the understanding of nitrogenase enzymes include the properties of V-type nitrogenase[72;73;74], the order of the catalytic steps[75;76;77] and the essence of electronic transfer between metal clusters, and the role of ATP.[78;79;80]

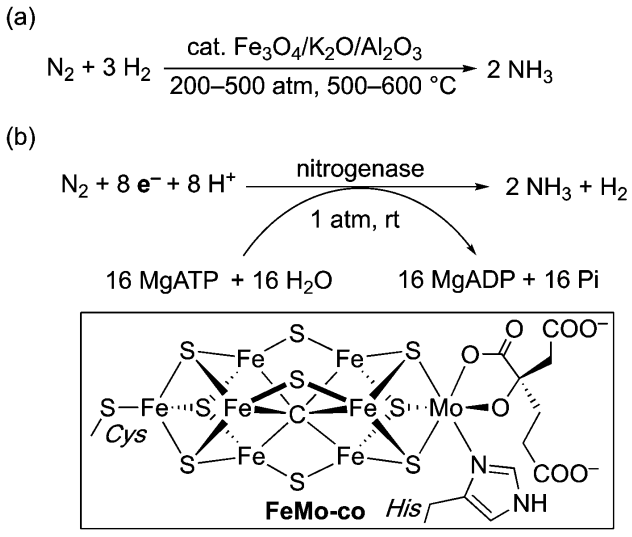


Figure 2.2: (a) Reaction scheme of the Haber-Bosch process (b) Reaction scheme of the FeMo cofactor active site in nitrogenase[5]

One of the most notable scientific breakthroughs in the field of nitrogen fixation was made in 1918 by Fritz Haber. Haber developed a way to produce ammonia using a heterogeneous catalyst, H_2 and atmospheric N_2 over iron.[81] In 1931, Carl Bosch revolutionized the process by augmenting it to an industrial level.[23] Consequently, it is famously known as the Haber-Bosch process and is still widely employed today. The significance of this discovery led to Haber and Bosch receiving Nobel Prizes for their novel contribution in the field of nitrogen fixation.[82] The Haber-Bosch process and other breakthrough methods involve reacting dinitrogen and hydrogen gas over a magnetite catalyst (Fe_3O_4) along with other various metal oxides.[6;81;5]

The Haber-Bosch process paved the way for increased global agricultural production in a world where many go hungry, yet the process is not quite as efficient as its biological

counterpart nitrogenase.[83] Figure 2.2 illustrates the different mechanisms used in the Haber-Bosh process and the MoFe cofactor in nitrogenase.[5] A major drawback in the Haber-Bosch process is the high pressure and temperature required under in order to overcome the high N_2 dissociation barrier at 225 kcal mol^{-1}, and the pure hydrogen source is derived from fossil fuel hydrocarbons.[84;85] Environmental damage is caused by the steam reformation of methane in the heterogeneous catalyst and accounts for most of the cost of the Haber-Bosch process.[86] Nitrogen fixation is estimated to be responsible for 1-2 percent of the world's total energy consumption per year.[87]

In addition to being an inefficient production process, it is estimated that a large portion of produced fertilizer is lost to the environment. In 2005, nearly 100 Tg N produced from the Haber-Bosch process was used for agricultural purposes and only 17 Tg N was consumed by humans.[88] One study indicated that nearly 40% of nitrogen fertilizer lost to the environment denitrifies and returns to the atmosphere as N_2.[89] Although dinitrogen is benign in the atmosphere, it represents about 1% of the global primary energy supply wasted in the production of fertilizers.[89] The increased production of reactive nitrogen has altered the balance of greenhouse gases and toposhperic ozone, affects acidity levels in soil and form secondary particle matter in the atmosphere, all of which negatively impact people and the environment.[23]

Inorganic compounds have been synthesized in an attempt to mimic the biological efficiency of the nitrogenase FeMo-co performing N_2 functionalization under ambient conditions in a homogeneous environment.[5] The biomimetic approach has led to research groups synthesizing complexes with a molybdenum active site.[90;91;92;6] Four of such complexes are shown in Figure 2.3.

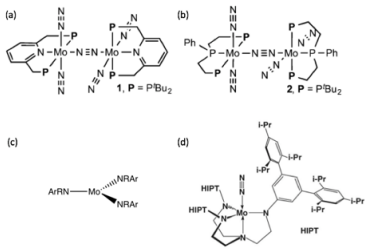
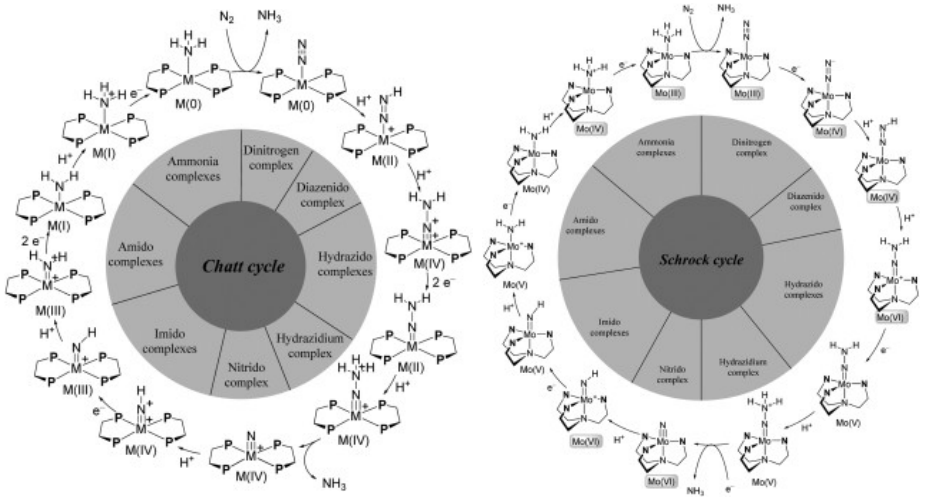


Figure 2.3: Synthesized molybdenum based complexes: (a) & (b) PPP-pincer catalysts by Nishibayashi (c) Mo-complex that cleaves the N_2 triple bond by Cummins (d) Schrock mononuclear Mo-catalyst[6]

Not all of the complexes in Figure 2.3 achieved N_2 functionalization by cleaving the N_2 bond. For example, in 1996, Laplaza and Cummins produced a dinuclear molybdenum system that forms two metal nitrido complexes via stretching of the N_2 bond (Figure 2.3(c)) .[93] Nishibayashi and coworkers studied molybdenum species with PNP-pincer and tridentate

triphosphine ligands and suggested that catalysis is performed via direct cleavage of the N_2 bond or by alternating protonation and reduction pathways.[5] Yandulov and Schrock proposed a catalyst that successfully fixated nitrogen and produced ammonia under ambient conditions with a coordinated tetradentate triamidoamine ligands with three hexaiopropylterphenyl (HITP) substitutions in a molybdenum system acting as a catalyst (Figure 2.3(d)).[30]



(a) Chatt Cycle[6] (b) Schrock Cycle[6]

Figure 2.4: Two proposed cycles for the catalytic formation of ammonia

One of the most prominently known mechanisms for N_2 functionalization is the Chatt cycle. The Chatt cycle proposes a mechanism involving activation and protonation with a mononuclear group VI dinitrgoen complex.[94] In the Chatt cycle, a dinitrogen species is attached to either a molybdenum or tungsten metal center that transforms to a d^0 oxidation state from a zero-valent species throughout the cycle shown in Figure 2.4(a). A hydrogen can interact with the electron-rich dinitrogen ligand on the metal species. This mechanism along with another well known mechanism known, the Schrock cycle, provide an understanding for possible ways nitrogen fixation can occur. The Schrock cycle proposes an oxidation of the molybdenum metal center from Mo(III) to Mo(IV) as shown in Figure 2.4(b).[95] The hydrogen source considered is 2,6-lutidinium tetrakis[3,5-bis(trifluoromethyl)phenylborate] ([LutH]Bar_4F) and decamethylchromocene ($CrCp_2^*$) as the reducing agent. The Schrock

catalyst shown in Figure 2.3(d) is activated via the protonation/reduction cycle proposed in the Schrock cycle.[6]

The ubiquity of molybdenum in many of the species studied and the catalytic activity of the MoFe cofactor are reasons for why we wish the study the binding activity of various molybdenum-nitrogen containing systems, and as a result, elucidate the electronic structure of the modality. To get a clear understanding of molybdenum and dinitrogen binding modalities, the study will focus on systems with 1-2 molybdenum sites and dinitrogen. A similar approach was used in 2006 by Cramer, Piecuch, and Gagliardi in the study of the Cu_2O_2 torture track. In this study, computational studies were used to elucidate the binding activity between multiple copper centers and dioxygen[96] Our goal is to use a similar approach to understand the nature of the moiety in the absence of a ligand field. We propose to begin by elongating the Mo-N and N-N bonds in small di-, tri-, and tetra-atomic systems. In doing this, we can gain a clearer understanding of the the impact of the binding modality on the energetics of the N_2 bond cleavage. Five models were proposed for this study

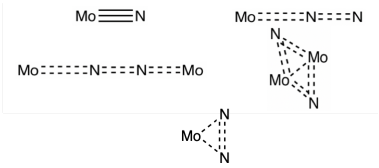


Figure 2.5: Proposed molybdenum-nitrogen based systems

The binding of dinitrogen, acting as a lewis base, to a metal atom, acting as a lewis acid, can be described as end-on, side-on, or a combination of the two. Figure 2.6 shows the various binding motifs typical of diatomic ligands. The d orbital of a transition metal and the p orbital(s) of the diatomic ligand overlap when having end-on and side-on geometries, as shown in the bottom of figure 2.6. The proposed molybdenum-nitrogen based systems mimic the geometries shown in figure 2.6 to investigate if these types of interactions occur between molybdenum and dinitrogen.[7]

For the purpose of this study, the binding interactions of a linear MoN_2 system is investigated. For end-on N_2 complexes, linear MNN binding is prominent, and therefore, will be considered in this study. End-on binding is facilitated by π-backbonding interactions from the d orbitals of the metal to the the π^* orbitals of N_2, which is due

to the symmetry and overlap of the interacting orbitals. The extent of this interaction varies based on the energies of the d orbitals and symmetry of the interacting orbitals. Typically, a low valent, relatively electropositive metal is better suited for backbonding than a highly electronegative metal. Additionally, the energy of the d orbitals from the metal dictates the amount of charge transfer from the metal to the diatomic ligand, and d orbitals with higher energies are better suited for transferring electron density in N_2 ligand. For N_2 ligand complexes, studies have shown that there is a trend in the type of species formed and the oxidation level of the metal. Metals with a lower oxidation state engage in stronger π-backbonding due to having more electrons and, therefore, higher orbital energies. The geometry of the metal center plays a large role in the electron distribution of complexes that bind to N_2. Adding ligands may affect the extent of N_2 activation and change the binding modes. Molybdenum is included with a number of transition metals (Ti, V, Cr, Zr, Nb, Hf, Ta, W, and Ac) that have been observed to bind and activate N_2 towards reactions.[7]

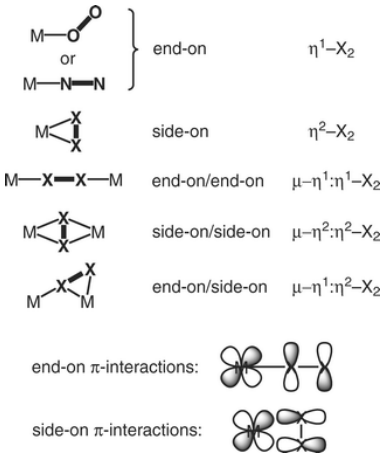


Figure 2.6: Diatomic ligand binding modes[7]

This system will focus solely on the linear MoN_2 system. Further research is currently being conducted in the Vogiatzis group on the remaining systems.

2.2 Methods

A class of electronic structure methods known as multi-reference (MR) methods were used to study the triatomic MoN_2 system. All calculations were performed with the quantum chemical software package MOLCAS.[97] Two methods, Complete Active Space Self-Consistent Field (CASSCF)[98;99] and Complete Active Space Perturbation Theory to the 2^{nd} order (CASPT2)[100] were used, providing static and dynamic correlation respectively. Dynamic correlation refers to the correlation in the movement of electrons, and static correlation describes the ground state of a wave function by use of multi-configurational self-consistent field (MCSCF) methods that take into account multiple determinants. The

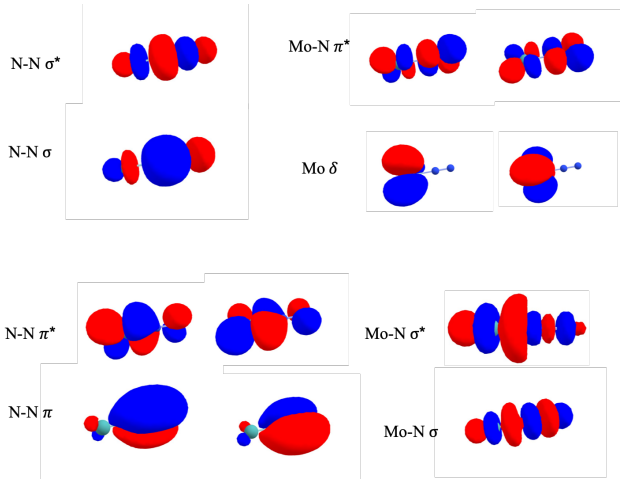


Figure 2.7: Illustration of the 12 molecular orbitals in the active space of this study

CASSCF notation representing n number of electrons in the active space located in m orbitals is given as CAS(n,m). The active space of MoN_2 was determined by choosing the orbitals that would impact on the binding activity of the molecule. For each nitrogen, the 2p orbitals were included, giving 6 electrons. The five 4d and the 5s electrons in molybdenum were chosen, giving 6 electrons for neutral Mo. Three oxidation states of molybdenum were included in this study, Mo(0), Mo^{2+}, and Mo^{3+}. For each model, all possible spin states were tested. For the neutral MoN_2 system, Mo has a valence electron configuration of $5s^1 4d^5$ and can have a singlet, triplet, or quintet spin state. The CASSCF notation for this model is CAS(12,12). Mo^{+2} has a valence electron configuration of $5s^0 4d^4$, and can have a spin state of a singlet, triplet, or quintet; the CASSCF notation is CAS(10,12). Likewise, the Mo^{3+} species has a valence electron configuration of $5s^0 4d^3$. The molecular model can have a spin state of a doublet or quartet, and the CASSCF notation is CAS(9,12). Below is an illustration of the molecular orbitals in the CAS.

The distances were systematically scanned, and single point energies were calculated for each step. The scan was performed by keeping the middle nitrogen in the linear Mo-N-N system frozen in space (coordinates x=0, y=0, z=0). The distance of the second nitrogen was changed each calculation by 0.025 Å in the range from 1 Å to 3 Å. Once a whole cycle of distances were completed for the outer nitrogen atom, the molybdenum atom's distance was incremented by 0.025 Åin the range from 1.4 Å to 2.5 Å. Therefore, for each change in distance to the molybdenum atom, one cycle of distance changes in the outer nitrogen was

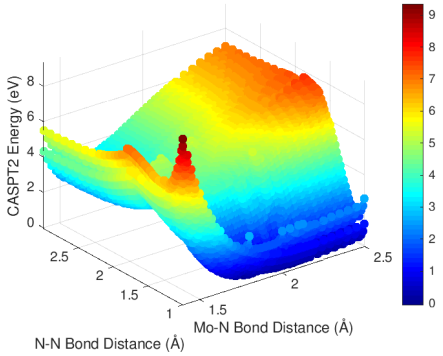
performed. Using Matlab, three-dimensional potential energy surface plots were made with the distances on the x- and y-axis and the CASPT2 energies on the z-axis (figures shown in the next section).

The triple-ζ, valence polarized, extended relativistic atomic natural orbital (ANO-RCC-VTZP) basis sets were implemented in this study.[101] The ANO-RCC basis sets are contracted using the Douglas-Kroll Hamiltonian and are useful in calculations where scalar relativistic effects are included.[102;103] The scalar relativistic effects were calculated using the Douglas-Kroll 2nd order Hamiltonian. Relativistic effects become significant after the second row on the periodic table and may be important for molybdenum. Both imaginary[104] and IPEA[105] shifts were implemented in all CASPT2 calculations. The purpose of the imaginary level shifts is to remove unwanted energy contributions from virtual orbitals that often arise with a transition metal. Introducing an imaginary shift effectively removes the weakly coupled "intruders" that cause singularities that look like spikes in the potential energy curve. An IPEA shift is added due to a systematic error in the HF method which underestimates bond energies and overestimates spin state differences. The IPEA shift modifies the energies of the active space orbitals to align more closely with ionization and electron affinity energies.

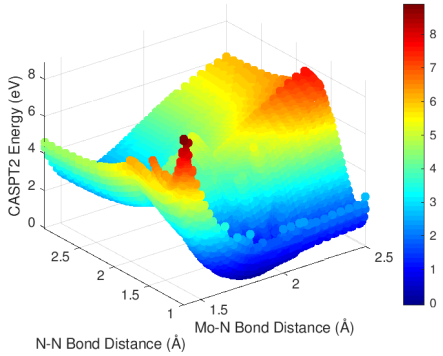
For this report, calculations using the symmetry state A_1 will be discussed. Other symmetry states are currently being tested.

2.3 Results and Discussion

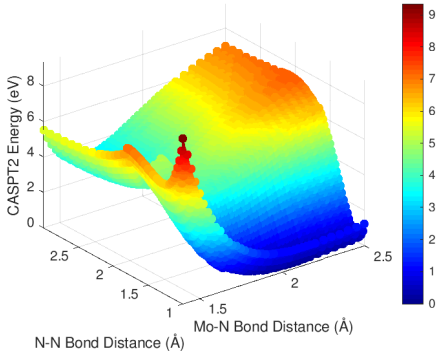
Eight sets of calculations were performed on the linear MoN_2 species. These varied in formal charge/oxidation states with a Mo(0), Mo(II), and Mo(III) system, and various spin multiplicities were tested in each of the three models. In the models with varying formal charges, the electrons are treated as being taken from the molybdenum atom. Singlet, triplet, and quintet spin states were calculated for both the neutral and $[MoN_2]^{2+}$ system. For the Mo(III) system, the doublet and quartet spin states were considered. For each system, potential energy surface (PES) plots were made.



(a) MoN_2 singlet PES



(b) MoN_2 triplet PES



(c) MoN_2 quintet PES

Figure 2.8: Potential energy surfaces of MoN_2 with a color map indicating the range of height (CASPT2 energy) of the surface

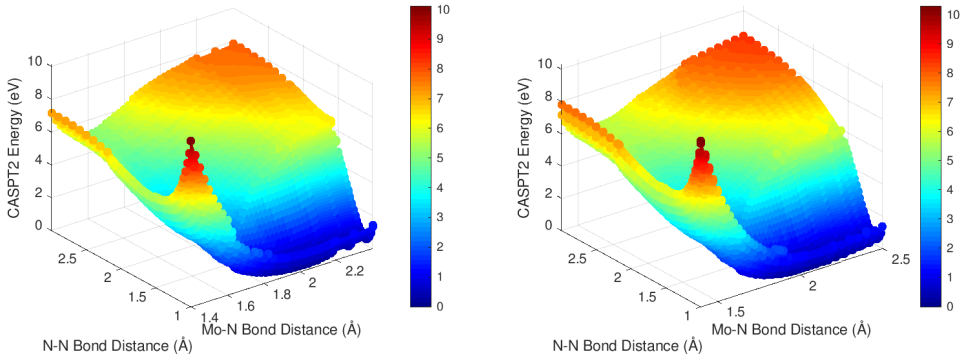
Mo Oxidation State	Spin State	Relative Minimum Energy (kcal mol^{-1})	Mo-N Distance (Å)	N-N Distance (Å)
0	S=0	26.7713	1.875	1.150
	S= 1	20.9038	1.850	1.150
	S= 2	0	2.075	1.100

Table 2.1: MoN_2 PES Data

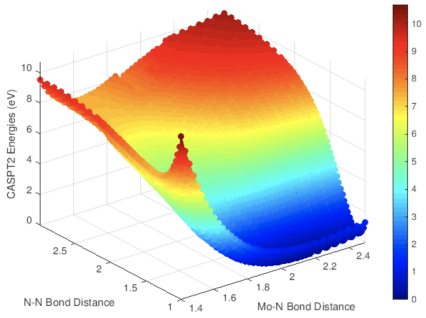
The Mo(0) systems were calculated with singlet, triplet, and quintet spin states, and each of the plots are shown in Figure 2.8 with (a), (b), and (c) corresponding to the singlet, triplet, and quintet states, respectively. All of the plots show similar trends– a high energy point when the three atoms are in very close proximity, relatively low energies when the

molybdenum is elongated and the N_2 is in close proximity, and an increase in energy as the N-N bond is elongated. Additionally, there is a local minima when the Mo-N bond distance is $\sim$ 1.5 and the N-N bond distance is $\sim$ 2.5 that is possibly a result of an interaction between Mo and N ions in close proximity as the N-N dissociates into two nitrogen ions. The point arising from the very close MoN_2 bond distances is the result unstable, high energy interactions of the molecules when forced together. These trends indicate that the MoN_2 species does not favor bonding because the system increases in energy when the N-N bond is elongated yet not when the Mo-N bond is elongated. Since bonding is a stabilizing effect, the N_2 system is more stable in its bound state than two free nitrogen ions.

The high spin quintet Mo(0) system was found to have the lowest minimum energy and the other two states are well separated. Interestingly, the bond lengths for the minimum are shown at 1.1 Å for N-N and 2.075 Å for Mo-N. Therefore, the most stable system with Mo(0) is the one that has an N-N bond length near that of stable N_2 (1.098 Å)[84] and an elongated Mo-N bond length. This further concurs with our conclusion that the MoN_2 system doesn't prefer a bound state.



(a) $[MoN_2]^{2+}$ singlet PES (b) $[MoN_2]^{2+}$ triplet PES



(c) $[MoN_2]^{2+}$ quintet PES

Figure 2.9: Potential energy surfaces of $[MoN_2]^{2+}$ with a color map indicating the range of height (CASPT2 energy) of the surface

Mo Oxidation State	Spin State	Relative Minimum Energy (kcal mol^{-1})	Mo-N Distance (Å)	N-N Distance (Å)
II	S=0	53.9722	2.050	1.100
	S=1	39.5043	2.125	1.125
	S=2	0	2.150	1.100

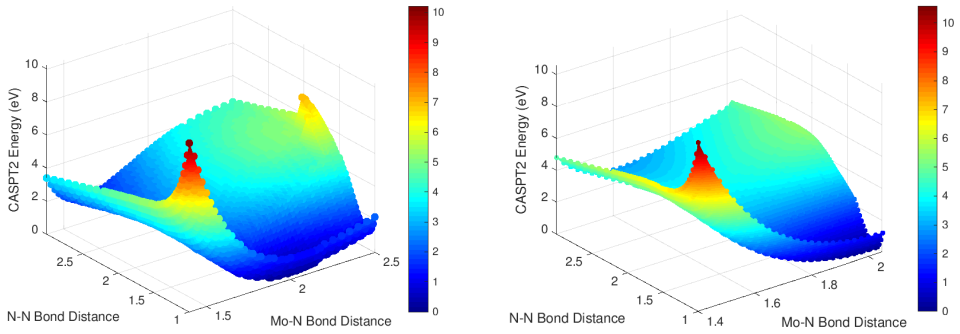
Table 2.2: $[MoN_2]^{2+}$ PES Data

The $[MoN_2]^{2+}$ system was analyzed with singlet, triplet, and quintet spin states which are shown in Figure 2.9 (a), (b), and (c), respectively. The d^4 molybdenum has a similar electronic structure to the previous model but has an empty s orbital. A similar general trend to the Mo(0) system is observed. As the N-N bond is kept as a stable length 1.0 Å, the elongation of molybdenum has little effect on the total energy. As the N-N bond is

increased, the total energy increases due to the N-N bond breaking and destabilizing the system. This data suggests that the system is not bound.

The relative minimum energy was calculated with the high spin quartet system being the most energetically stable. Given that molybdenum has a d^4 electronic structure, this seems reasonable given that there is no significant ligand field to cause broken degeneracy in the d-orbitals. The singlet and triplet states are very well separated at energy differences of 39.5 kcal mol^{-1} and 53.97 kcal mol^{-1}, respectively. The most stable N-N bond length for this system is 1.1 Å and 2.150 Å for the Mo-N bond. This is very similar to the Mo(0) system and further suggests that the most stable arrangement for this system is unbound with respect to the Mo-N bond with a stabilized N_2 species.

Interestingly, the HS species also has the largest gradient in the potential energy surface The scale in Figure 2.9(c) shows the graph's range from $0 \rightarrow 10$ eV. This system is the only system in this study to have this large of a relative energy difference. This suggests that the $S = 2$ system is more energetically reactive than other systems.



(a) Doublet (b) Quartet

Figure 2.10: Potential energy surfaces of $[MoN_2]^{3+}$ with a color map indicating the range of height (CASPT2 energy) of the surface

Mo Oxidation State	Spin State	Relative Minimum Energy (kcal mol^{-1})	Mo-N Distance (Å)	N-N Distance (Å)
III	S= $\frac{1}{2}$	31.7807	1.975	1.125
	S= $\frac{3}{2}$	0	2.050	1.125

Table 2.3: $[MoN_2]^{3+}$ PES Data

The $[MoN_2]^{3+}$ system has the highest formal charge, the least electrons, analyzed in this study. Figure 2.10(a) and (b) show the HS and LS $[MoN_2]^{3+}$ potential energy surface. An observable difference between the other two systems and this one in the potential energy plots is that $[MoN_2]^{3+}$ is not significantly affected in relative energy when the distances between atoms are increased. The system remains relatively similar at all bond lengths, especially in the high spin quartet. The general trend still holds for this system, albeit on a smaller scale. There is a still an increase in energy when the three atoms are extended over 2 Å apart, and the energy is at the minimum when the Mo-N bond distance is stretched and the N-N distance is close to its normally observed bond length. From these two plots, it can be concluded that the energetic interactions in the MoN_2 system are weaker than those in the previous two models, and that the Mo^{3+} ion is relatively stable compared to Mo(0) and Mo^{2+}.

2.4 Conclusions

In this work, an in-depth study of the binding activity of MoN_2 was performed by applying multiconfigurational wave function theory. Our calculations revealed the binding modalities of MoN_2 through potential energy surfaces made from elongating interatomic distances. Various spin states and oxidation states of molybdenum were tested. The results presented here suggests that the linear MoN_2 moiety does not favor binding.

Each plot depicts the relative change in energy as the bond distances between the middle nitrogen and the molybdenum and outer nitrogen expand. The increase in energy as the N_2 distance expands suggest that this system does not favor binding with molybdenum.

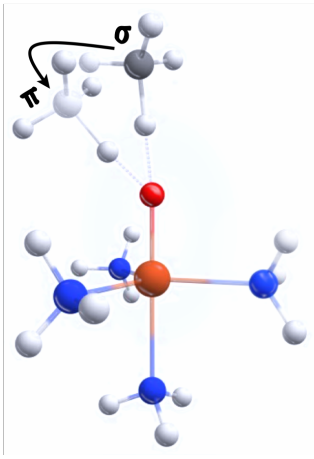
Likewise, N_2 is more stable than two free nitrogen ions, and this behavior is observed increase of energy in the system when the N_2 bond distance is elongated. The Mo-N bond distance does not have a significant affect the energy when the N_2 is near its equilibrium bond length. A pronounced local minimum is observed in the potential energy surfaces of MoN_2 and more subtely in the potential energy surface of $[MoN_2]^{3+}$ and $[MoN_2]^{2+}$. The local minima occur near an Mo-N distance of 1.6 Å and an N-N distance of 2.5 Å. One explanation to this could be an interaction between the molybdenum and nitrogen ion when bond dissociation occurs between the N_2 species. The data suggests that, at times, a diatomic species is present in the form of molybdeum-nitrogen or dinitrogen, but not as a triatomic system.

The observation of an unbound system further supports the hypothesis that the ligand field is responsible for creating a suitable binding environment. From our data the Mo(0) species is not able to bind to N_2 and perform nitrogen fixation, yet for systems that undergo the Chatt cycle, we see that Mo(0) is essential for nitrogen fixation to occur. In the Chatt cycle, a metal complex makes use of an electron-rich ligand coordinated to a zero-valent molybdenum. Proton sources are able to attack the complex and in a stepwise fashion, protonate the dinitrogen complex affording diazenido (MN=NH), hydrazido (MN–NH2), and hydrazidium (MN–NH3) intermediates.[6] It can be concluded that the absence of electron-rich ligands hinders the MoN_2 system from binding and being able to undergo a catalytic cycle.

Further studies are being conducted to investigate the binding activity on larger systems containing molybdenum and nitrogen.

Chapter 3

Computational Studies on the Electronic Structure of Iron(IV)-Oxo Transition States



3.1 Introduction

The role of transition metal mediated oxidation of alkanes has proven to be one of the top challenges in various branches of chemistry, biology, and chemical engineering.[106;3] Consequently, the elucidation of the mechanistic aspects that lead to the catalytic conversion of methane to methanol has received considerable interest over the last decade.[107;8] This is primarily since that nearly 40 million metric tons of methanol processed each year are

converted into everyday products from fuels to shampoos.[108] Since current industrialized processes are unable to convert methane to methanol directly, the role of metal oxides in a thermodynamically favorable, direct catalytic system is currently being investigated.[3] The complexities associated with the seemingly simple activation and functionalization of organic molecules has driven efforts focused on uncovering the elementary steps of the catalytic cycle.

An initial challenge in creating an energy efficient catalytic cycle is the activation of the C-H bond of methane under ambient conditions. The initial barrier is afforded by the intrinsic properties of the hydrocarbon, including low electron affinity, the significant energy gap between the highest occupied molecular orbital (HOMO) and lowest unoccupied molecular orbital (LUMO), the lack of a dipole moment, and the limited polarizability of methane.[8] "Bare" metal oxides have been proposed as the basis for species capable of conducting homolytic C-H bond activation.[109;110;111] (3.1)

$$MO\cdot + H - CH_3 \rightarrow MO - H + CH_3\cdot \tag{3.1}$$

Several suggestions have been made for a mechanism involving the activation of methane by a reactive a metal species.[112] The Lunsford method 3.1 is one of such proposed catalytic mechanisms and involves the oxidative coupling of methane via a lithium metal oxide.[113]

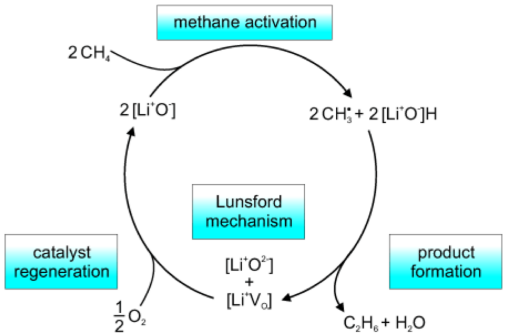


Figure 3.1: Lunsford catalytic scheme[8]

Although much debate has been made on the nature of the active metal oxide species, the favorable homolytic cleavage of the C-H bond at ambient temperature suggests that these systems may be fundamental for overcoming the rate-determining step of the activation of methane.[8]

Ubiquitous in nature, high-valent heme and non-heme iron-oxo molecules are key oxidizing intermediates in an array of biological reactions. Enzymes containing dinuclear and mononuclear iron have been experimentally observed to perform hydroxylation on an unactivated C-H bond. For example, methane monooxygenase enzymes (MMO's) found in methanotrophic bacteria successfully and efficiently achieve methane to methanol oxidation under ambient conditions.[114]. Additionally, α-ketoglutarate[115], isopenicillin N-synthase (IPNS)[116], 4-hydroxymandelate synthase[117], and tyrosine hydroxylase[118] are enzymes constituted of non-heme iron cofactor units that promote oxidative transformations of aliphatic bonds. Iron(IV)-oxo intermediates are thought to be key for hydrogen abstraction, resulting in an Fe(III)-OH complex. Figure 3.2 illustrates a general proposed scheme involving a high-valent iron-oxo intermediate.[9]

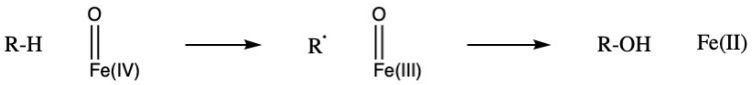


Figure 3.2: Hydroxylation scheme with a high-valent iron-oxo intermediate[9]

Biomimetic studies aimed at elucidating the mechanisms of iron(IV)-oxo intermediates that oxidize hydrocarbon bonds have led to the synthesis of numerous model complexes.[11;119;120;121;122] In the 90's, T.J. Collins and coworkers produced various biologically inspired tetramido macrocyclic ligands known as TAMLs.[123] Collins is recognized as the forerunner in the study biomimetic, high-valent iron complexes with non-heme ligands. Their successful characterization of a high spin iron(IV) complex led to new discoveries and an increased interest in the field.[124] The scarcity of model complexes that catalyze oxidative transformations led to a number of experimental

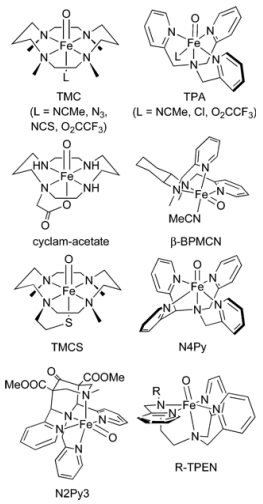


Figure 3.3: Synthesized iron(IV)-oxo complexes[10]

efforts that resulted in exciting experimental results. A sample of model complexes that have been produced in the last couple decades are shown in Figure 3.3.[10]

In 2007, Nam characterized biomimetic heme and non-heme iron(IV)-oxo model complexes, such as the one shown in Figure 3.4, and studied how different ligand environments affected their ability to undergo oxygenation reactions.[11] Experimental studies express interest in understanding the roles of ligands in directing and tuning the oxidizing ability of iron-oxo intermediates.

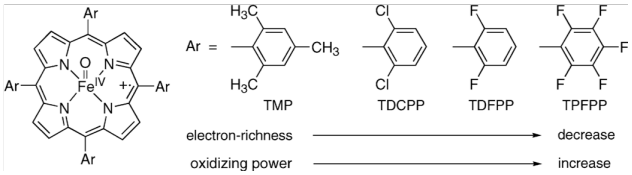


Figure 3.4: Iron-oxo porphyrin complex study by Nam, where Ar is a functional ligand[11]

Nature shows a preference for an Fe(IV)-oxo coordination environment that gives rise to a highly reactive, high-spin state of a quintet (S = 2).[3] The challenge to duplicate the reactivity of an iron-oxo quintet complex has led to investigations of metal-organic frameworks (MOFs).[125;126;127] MOFs consisting of site-isolated iron centers within a trigonal bipyramidal environment have been shown to activate C-H bonds successfully.[128] Spectroscopic and computational studies have verified the stabilization of the highly reactive iron(IV)-oxo intermediate due to weak ligand field surrounding deposited iron cations in porous materials.[129;130;131;132] Conversely, non-heme complexes with an iron center appear to prefer an intermediate spin state (triplet, S = 1).[11;133;] Various approaches have been taken to synthesize complexes with a ligand field that is conducive to a high spin iron(IV)-oxo center.[128;134;135;136]

One challenge accompanied with synthesizing a catalytic iron(IV)-oxo complex is the observation of a two state reactivity (TSR) scheme leading to a change in spin states in triplet spin complexes during the hydrogen abstraction step.[137] A TSR scheme results in a triplet to quintet spin state change that lowers the activation barrier and has been argued to decrease the reactivity of the triplet complex.[138] Meyer and coworkers synthesized a triplet complex with a strong ligand field resulting in the complex having a large triplet-quintet gap that did not allow a spin transfer. The highly reactive nature of this complex is a result of averting the TSR scheme.[139;140;141]

Two additional challenges involved with producing a highly reactive catalyst include steric hindrance and self-oxidation paths characteristic of iron-oxo complexes.[142] Detailed spectroscopic and computational studies have highlighted two possible pathways available to the iron(IV)-oxo complex. One is self-oxidation and causes the disintegration of the catalysts via a π channel. The other is the desired C-H activation of an aliphatic substrate by the iron(IV)-oxo active site via the σ-channel.[3]

Past studies have determined the frontier molecular orbitals (FMO's), the electronic structure that controls the activity of the complex, of various high-spin (HS) and low-spin (LS) Fe(IV)-oxo complexes.[143;142;141;144;145;146;147;148] The FMO's directly influence the selective reactivity, and the spin changes the complex undergoes during C-H activation. Different aliphatic bond activation mechanisms result from the changes in electronic structure and bond elongation that occurs in the iron(IV)-oxo $\rightarrow$ iron(III)-oxyl species transition.[149] A diagram of the valence bond orbitals belonging to FeO^{2+} is shown in Figure 3.5.[3] The MO diagram depicts the σ, π, non-bonding ($d_{x^2-y^2}$/ d_{xy}), π^*, and σ^* orbitals in an FeO^{2+} species.

Available to iron(IV)-oxo species with specific ligand environments, the highly reactive σ- and π-channels are observed to lead to different electron distributions in the FMOs. Both of these channels show high reactivity because they form an oxyl species (Fe(III)-$O^{\cdot-}$) in the transition state. The first of the four possible channels correspond to the promotion of an electron from the σ bonding orbital to the σ^* antibonding orbital. (Figure 3.6)[3] In this mechanism accessible by the ground state iron(IV)-oxo intermediate, hydrogen abstraction is made possible due to an excitation from the σ orbital. The σ orbital is polarized in the direction of the oxygen, while the σ^* is polarized

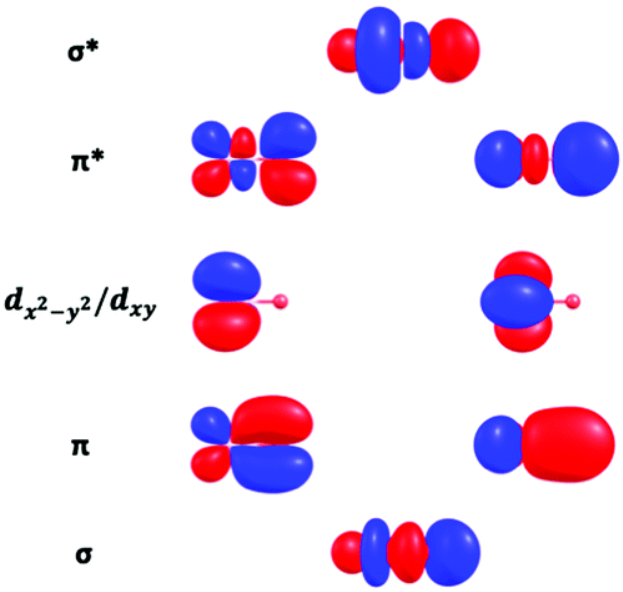


Figure 3.5: Valence molecular orbital diagram of FeO^{2+}[3]

towards the iron. Both the σ orbital and the σ^* orbital become singly occupied upon the $\sigma \rightarrow \sigma^*$ excitation. At this point the oxygen has adopted radical oxyl character ($O^{2-} \rightarrow O^{\cdot -}$), and hydrogen abstraction is favorable. The $\sigma \rightarrow \sigma^*$ excitation is termed the σ-mechanism because the σ orbital is responsible for the oxyl character and hydrogen abstraction. The second possible mechanism is the excitation from the doubly degenerate π orbitals. The competitive excitation state of the doubly degenerate π orbitals (E symmetry) results in one electron from either π orbital promoting to the empty σ^* orbital. This leaves one π orbital filled and the other singly filled, while the the σ^* becomes singly filled. The oxo species develops the reactive oxyl character once this excitation occurs. The oxyl character is primarily due to the $\pi \rightarrow \sigma^*$ excitation and is known as the π-mechanism. Figure 3.6 shows the four different possible MO diagrams that result from a quintet and triplet spin state in the molecule. The MO of an iron(IV)-oxo complex with a near-trigonal pyramidal is represented in Figure 3.6 (a) and shows preference for a quintet spin state, $^5\sigma$ and $^5\pi$. Conversely, Figure 3.6 (b) illustrates the MO diagram of a near-octahdral Fe(IV)-oxo complex, with a preferred triplet spin state as a consequence of the symmetry.

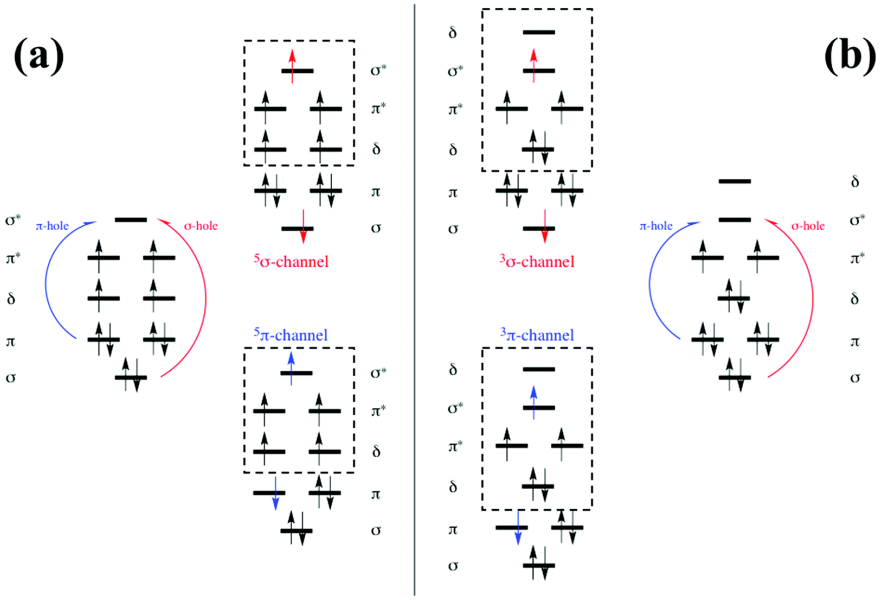


Figure 3.6: Four possible σ and π channels of Fe(IV)-oxo with (a) near-trigonal pyramidal field of an S = 2 species and (b) near-tetragonal field of an S = 1 species[3]

The mechanistic steps and the overall reaction is a compound result of the electronic structure and stereochemistry of the complex. The change in energy from the σ- and π-mechanisms are largely dependent on the ligand field. The energy gap (ΔE_{orb}) ($\pi^* \rightarrow \sigma^*$ / $\delta \rightarrow \sigma^*$) is affected by the strength of the ligand field, with weaker ligands having a lower average Δ E_{orb} than of strong ligand fields.[12] In a study by Shalk *et al.*, the exchanged enchanced reactivity of the σ- and π-channels in iron-oxo molecules was investigated by using models with nitrogen and substituted ligands. The effects of the ligand field and spin state on the σ- and π-paths are shown in Figure 3.7.[12]

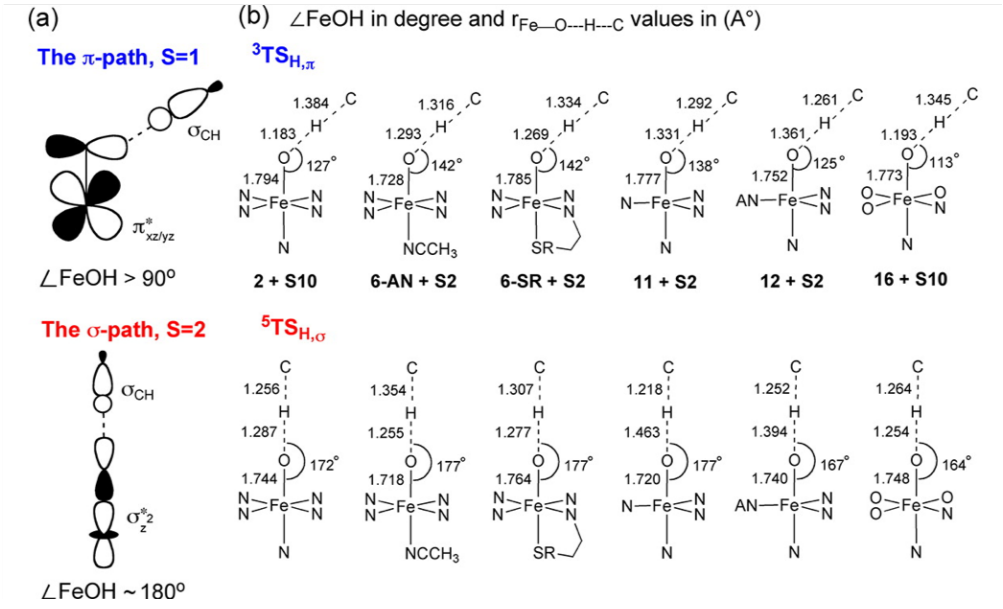


Figure 3.7: (a) Orbital overlap predictions of $^3TS_\pi$ and $^5TS_\sigma$ and (b) hydrogen abstraction TS geometries[12]

The transition state (TS) favors the channel that results in the highest amount of overlap between the σ orbital of the C-H molecule for hydrogen abstraction. Therefore, a ^{3}TS is predicted to prefer a lateral approach to maximize the σ_{CH}-$\pi^*_{xz/yz}$ overlap, and a ^{5}TS is predicted to promote a linear Fe-O-H angle to maximize the σ_{CH} - $\sigma^*_{d\ z^2}$ overlap.[150] Typically, longer Fe-O bond distances prefer hydrogen abstraction via the π-channel and shorter bond distances are observed in σ-mechanisms, as predicted in Figure 3.7. In certain complexes, for example the non-heme enzyme SyrB2, both $^5\sigma$- and $^5\pi$- channels are reactive and have different roles. The $^5\sigma$-mechanism promotes hydroxylation while the $^5\pi$-mechanism promotes halogenation.[151;145] Other highly reactive complexes perform homolytic C-H bond

activation by both σ- and π-mechanisms. For example, tetracarbene (S = 1) is accessible by $^3\sigma$ and $^3\pi$ channels[141], and AlkB enzymes activate an aliphatic bond by both the $^5\sigma$ and $^5\pi$ channels.[152]

Our group is currently examining factors that are contingent on the electronic structure of Fe(IV)-oxo sites. This project aims to analyze the geometrical components affecting the catalytic activity of these active sites by investigating the accessibility of the oxo/oxyl atom and the shielding effects caused by ligand functional groups. The molecular orbital energies and the availability of the σ- and π-channels give insight into the accessibility of the active site. The estimation of the oxo/oxyl atom exposure can be calculated by inserting a probe sphere (methane) into the crystal structures of Fe(IV)-oxo molecules and calculating the overlap between the methane and the ligands. In this study, the σ- and π-pathways of high-valent iron(IV)-oxo complexes capable of functionalizing aliphatic bonds are elucidated through the use of high-level wave function theory methods including CASSCF and CASPT2 as well as density functional theory (DFT). The system investigated in this project is $[Fe(O)(NH_3)_4]^{+2}$.

3.2 Computational Details

The starting geometry was taken from the supporting information in Andrikopoulos, *et al.*[153]

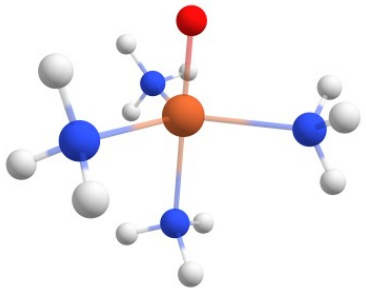


Figure 3.8: Model complex used in this work: $[FeO(NH_3)_4]^{2+}$, near-C_{3v}, (Fe: orange, N: blue, O: red, H: white)

The TURBOMOLE[154] quantum chemistry program package was used for density functional theory (DFT) calculations. DFT calculations were performed using the B3LYP-D3(BJ) functional[155] and def2-TZVPP[156;157] basis set for all atoms. B3LYP is a common functional

due to its ability to accurately predict molecular properties, but B3LYP alone does not always reliably depict noncovalent interactions.[158] Therefore, dispersion corrections can be added to the B3LYP funcitonal (D3). Additionally, Becke and Johnson damping (BJ-damping) is added with the D3 dispersion correction to improve results for nonbonded distances.[159] The resolution-of-identity (RI) approximation is a scheme used for solving calculations quicker and was also applied to these calculations.[160] This level of theory was used for all geometry optimizations and single point calculations.

The basis set was determined by comparing the numerical result with the number of basis functions in each basis set, which scale with computational time, for def2-SVP, def2-TZVP, def2-TZVPP, def2-TZVPPD, and def2-QZVP.[156;157;161] A single point DFT calculation was performed on the transition state complex for basic comparison. These basis sets correspond to split valence polarization, valence triple-ζ polarization, valence triple-ζ with two sets of polarized functions, valence triple-ζ with two sets of polarization functions and a set of diffuse functions, and valence quadruple-ζ polarization, respectively. As expected, the basis set increased, so did the calculation time. The scaling between the def2-TZVPP and def2-TZVPPD basis is about a magnitude larger. When taking this into consideration along with the comparable energies, the def2-TZVPP basis set was chosen as the most practical for this study.

Stationary point calculations were performed for the TS models. Stationary point calculations search for a zero gradient on the potential energy surface. A first order saddle point indicates a TS has been found. Since vibrational frequencies are essentially the square root of the curvature, one negative or imaginary frequency indicates a TS. On the other hand, an all positive Hessian matrix, no negative frequencies, indicates a minimum has been found.[154] The quasi-Newton-Raphson method is used in TURBOMOLE's TS optimization to maximize the energy along one of the Hessian eigenvectors and minimize the rest.[162] A grid size of four as opposed to three was used for increased numerical accuracy. An increased grid size increases the amount of integration points taken in the calculation.[163] $[FeO(NH_3)_4]^{2+}$ is observed to have a near-C_{3v} symmetry, but no symmetry was specified for calculations in this study.

Once the reactant model geometries and SCF energies successfully converged, the Fe-O-H angle was iteratively adjusted by 5°along the z-axis. Once adjusted, a TS optimization was performed where the angle between the Fe, O, and H of methane atom was constrained. An additional set of calculations were performed using the geometry of the various Fe-O-H angles but without applying any constraints.

Additionally, MR methods were used to study $[FeO(NH_3)_4]^{2+}$ and the two optimal σ- and π-channel TS models from the unconstrained calculations. The calculations were performed with the quantum chemical software package MOLCAS.[97] Two methods, Complete Active Space Self-Consistent Field (CASSCF)[98;99] and Complete Active Space Perturbation Theory to the 2nd order (CASPT2)[100] were used, providing static and dynamic correlation, respectively. As discussed in the previous chapter the notation for the active space orbitals and electrons is denoted as CAS(n,m), with n representing the number of electrons in the active space and m as the number of orbitals located in the active space. For the TS models, CAS(12,10) was used. The 12 electrons chosen correspond to the d^4 shell of Fe(IV), 2 electrons from the p_z shell from C-H of methane, and 6 electrons from the p shell of O^{2-}. The five d orbitals of Fe, the three p orbitals of O, and the p_z orbital of methane were considered integral to methane activation by $[FeO(NH_3)_4]^{2+}$ and considered in the molecular active space. In total, there are only 9 orbitals mentioned; a tenth is added to ensure that our active space is what we expect and is an unoccupied (virtual) orbital. For the $[FeO(NH_3)_4]^{2+}$ model, an active space of CAS(10,8) was chosen. The same logic as discuessed for the TS active space applied, but without the methane contribution and the inclusion of the unoccupied orbital.

Similar to the previous chapter, the triple-ζ, valence polarized, extended relativistic atomic natural orbital (ANO-RCC-VTZP) basis sets were used in this study.[101] The ANO-RCC basis sets are contracted using the Douglas-Kroll Hamiltonian and are useful in calculations where scalar relativistic effects are included.[102;103] Use of the Douglas-Kroll 2^nd order Hamiltonian accounts for scalar relativistic effects, which become significant after the second row on the periodic table. Both imaginary[104] and IPEA[105] shifts were implemented in all CASPT2 calculations. These shifts were introduced as corrections for our model and their significance was previously discussed in the last chapter.

3.3 Results and Discussion

DFT calculations on the iron(IV)-oxo complexes were performed to find the ground spin state. For the near trigonal bipyramidal $[FeO(NH_3)_4]^{2+}$ complex, the lowest energy state was found to be the high spin quintet.

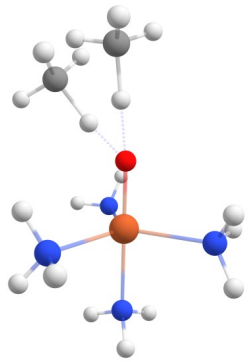


Figure 3.9: $[FeO(NH_3)_4]^{2+}$ + CH_4 TS σ- and π- channel angles (Fe: orange, N: blue, O: red, H: white, C: grey)

In the next step, we began calculations for transition states using the spin state of the reactant complex. Two sets of calculations were performed: a set of calculations with the Fe-O-H angle constrained and another using same starting geometry as the constrained calculations but without any constraints. Results from the calculations where the starting geometry set the Fe-O-H bond angle without constraints highlighted two available activation pathways, the σ- and the π-channel. The two different angles that represent the σ- and the π-pathways are shown in Figure 3.9, with the σ-channel represented by the 179° Fe-O-H angle and the π-channel shown with the 134° angle.

For complexes with a starting geometry of an Fe-O-H angle between 104° and 119°, the π-channel at 134.07° was preferred. If the starting geometry of the Fe-O-H angle on the z-axis was between 124° and 179°, the σ-channel at 179.41° was favored instead. The calculations with the lowest energies corresponding to the σ- and π-channel were taken as the optimal angles. Table 3.4 and 3.5 shows the data obtained from the unconstrained TS optimizations of $[FeO(NH_3)_4]^{2+}$. The energy gap between the lowest energy σ-channel and lowest energy π-channel is 7.529 kcal mol^{-1}. The activation energy was calculated at 8.82 kcal mol^{-1} for the σ-channel and 16.35 kcal mol^{-1} for the π-channel.

Table 3.1: Unconstrained TS model results for $[FeO(NH_3)_4]^{2+}$

Original Fe-O-H Angle	94	99	104	109	114	119
Relative Δ E (kcal mol^{-1})	7.531	7.529	7.531	7.534	7.537	7.537
Final Fe-O-H Angle	134.24	134.07	133.91	133.82	133.82	133.96

Table 3.2: Unconstrained TS model results for $[FeO(NH_3)_4]^{2+}$

Original Fe-O-H Angle	124	129	134	139	144	149	154	159	164	169	174
Relative Δ E (kcal mol^{-1})	0.009	0.003	0.000	0.004	0.038	0.002	0.006	0.007	0.009	0.008	0.005
Final Fe-O-H Angle	178.94	179.21	179.41	179.39	178.65	179.40	179.63	179.66	179.60	179.52	179.54

The optimized geometries from the $[FeO(NH_3)_4]^{2+}$ complex, σ-TS, and π-TS DFT calculations were used for a single point MR calculation. MR methods give insight into the nature of the active space orbitals by both visualization and fractional occupation numbers. The images were created through the ChemCraft[164] visualization software. The MOLCAS active space orbitals were utilized to create a molecular orbital (MO) diagram illustrating the σ- and π-channels. Figure 3.10 shows the molecular orbital diagram for the $[FeO(NH_3)_4]^{2+}$ complex.

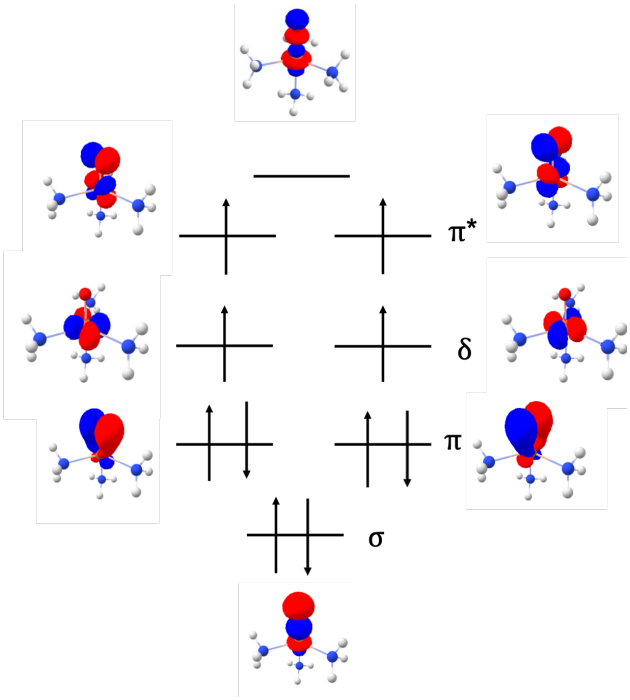
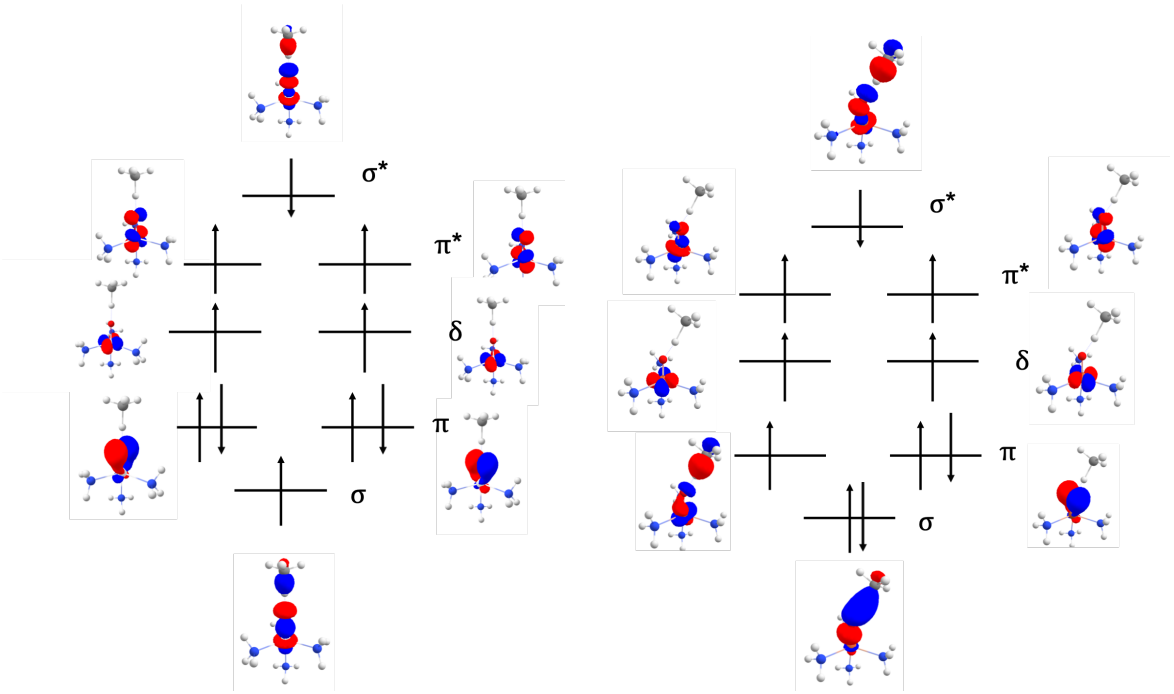


Figure 3.10: $[FeO(NH_3)_4]^{2+}$ molecular orbital diagram

The MO diagram corresponds to a high-spin quintet ground state of $[FeO(NH_3)_4]^{2+}$. Three orbitals are doubly occupied, the σ orbital and the two bonding π orbitals. Two non-bonding orbitals along with both of the π^* orbitals are singly filled. The ground state molecular orbital diagram is helpful for analyzing the TS diagrams in Figure 3.11. Table 3.3 shows relevant distances and angles from the optimization of the $[FeO(NH_3)_4]^{2+}$ structure.

Table 3.3: Optimized Geometry Analysis of $[FeO(NH_3)_4]^{2+}$

Distances (Å)	
Fe-O	1.61
N_{eq}-Fe (avg)	2.11
N_{ax}-Fe	2.14
Angles (°)	
O-Fe-N_{ax}	179.50



(a) σ-TS $[FeO(NH_3)_4]^{2+}$ + CH_4 (b) π-TS $[FeO(NH_3)_4]^{2+}$ + CH_4

Figure 3.11: Molecular orbital diagrams of the σ- and π-TS species

From the σ-TS complex shown in Figure 3.11(a), the fractional occupation number of the σ orbital is given at 1.6816 while the σ^* has a fractional occupation of 0.3297. Conversely, both π orbitals have occupation number near 2.0 (1.9467 and 1.9618), signifying double occupancy. In the π-TS model, the σ orbital shows a fractional occupancy of 1.9843, a doubly occupied orbital. The π orbitals show fractional occupations of 1.9883 and 1.4694 and σ^* at 0.5443. When comparing the σ- and π-TS species, it is clear that there is a difference in electron arrangement from the fractional occupation numbers. This further supports the hypothesis that two TS channels are available for hydrogen abstraction of the methane.

For the purpose of elucidating the σ- and π-channels, constrained Fe-O-H angle calculations were performed and Tables 3.4 and 3.5 below show the distances and angles along with the two lowest energy models from the unconstrained calculations for comparison. The models labeled π-TS and σ-TS represent the two optimal models from the unconstrained calculations. A trend in the bond length data is seen between the models with constrained Fe-O-H angles in the range of 99°to 124°and 129°to 179°and is similar to the trends between the σ- and π-channel preference in the unconstrained models. Additionally, the elongation

of the Fe-O bond is characteristic of the π-channel. The adverse effect is observed for the O-H and N_{ax}-Fe bond lengths in the σ-channel. The O-H bond length for complexes that favor the σ channel are $\sim$0.2 Å longer on average and the N_{ax}-Fe bond lengths are longer by $\sim$0.12 Å. In relation the $[FeO(NH_3)_4]^{2+}$ species (Table 3.3), the Fe-O bond length is extended in both TS mechanisms. The N_{ax}-Fe bond length in the π-channel models are very similar to the $[FeO(NH_3)_4]^{2+}$ species, but the σ-channel models are elongated $\sim$ 0.1 Å, showing that the stretch along the z-axis is characteristic to the σ-channel TS. The O-Fe-N_{ax} angle for $[FeO(NH_3)_4]^{2+}$ and the σ-channel models are very similar, while the π-channel deviates slightly from 179°. This is possibly a result of the optimal Fe-O-H angle of the π-channel being near 134°.

Table 3.4: Constrained TS model results for $[FeO(NH_3)_4]^{2+}$, π-channel

Models	π-TS	104	109	114	119	124
Distances (Å)						
Fe-O	1.73	1.74	1.73	1.73	1.73	1.73
O-H	1.24	1.27	1.26	1.26	1.26	1.25
C-H	1.28	1.28	1.28	1.28	1.28	1.28
N_{eq}-Fe (avg)	2.13	2.12	2.12	2.12	2.12	2.13
N_{ax}-Fe	2.15	2.12	2.12	2.13	2.13	2.14
Angles (°)						
O-Fe-N_{ax}	173.98	176.56	176.07	175.59	175.12	174.65
O-H-C	168.96	167.78	168.05	168.02	168.02	168.13

Table 3.5: Constrained TS model results for $[FeO(NH_3)_4]^{2+}$, σ-channel

Models	σ-TS	129	134	139	144	149	154	159	164	169	174	179
Distances (Å)												
Fe-O	1.70	1.70	1.70	1.70	1.70	1.70	1.70	1.70	1.70	1.70	1.70	1.70
O-H	1.40	1.48	1.47	1.46	1.45	1.44	1.43	1.42	1.42	1.41	1.41	1.40
C-H	1.21	1.17	1.18	1.18	1.18	1.19	1.19	1.20	1.20	1.20	1.21	1.21
N_{eq}-Fe (avg)	2.15	2.15	2.15	2.15	2.15	2.15	2.15	2.15	2.15	2.15	2.15	2.15
N_{ax}-Fe	2.27	2.24	2.25	2.25	2.25	2.26	2.26	2.26	2.27	2.27	2.27	2.27
Angles (°)												
O-Fe-N_{ax}	179.91	179.89	179.86	179.62	179.41	179.38	178.79	178.96	179.21	179.43	179.68	179.72
O-H-C	179.83	163.42	165.53	167.69	169.67	171.67	173.57	175.30	176.71	177.89	178.86	179.69

3.4 Conclusion

In this work, we have completed an in-depth characterization of the σ- and π-channel in the TS of the $[FeO(NH_3)_4]^{2+}$ + CH_4 system by applying both DFT and MR methods. Our calculations revealed the electronic effects of an iron-oxo coordinated wih NH_3 ligands in a trigonal bipyramidal geometry and a quintet ground state. The trigonal bipyramidal geometry induces splitting in the molecular orbital energies with four unpaired electrons occupying the non-bonding δ and the π^* molecular orbitals. Therefore, a relatively weak ligand field is present in the complex. We analyzed the structural and mechanistic differences in the reaction channels of the Fe(III)-oxyl radical TS species involved in C-H activation. Our results imply that the ligand field of biomimetic sites can be adjusted to favor the σ- or π-channel an iron(IV)-oxo complex, leading to successful functionalization of an aliphatic bond.

The σ- and π-channels were elucidated through the TS optimizations of both the constrained and unconstrained geometries from $[FeO(NH_3)_4]^{2+}$ + CH_4. DFT calculations were performed first. From the unconstrained search resulted two clear TS pathways, one with an Fe-O-H angle near 179° and the other around 134°. The two optimal calculations corresponding to the σ- and π-channels were analyzed along with DFT TS optimizations using Fe-O-H constrained angles varying by 5°. By doing this, we were able to get a better understanding of the characterstics of the σ- and π-channel of the tetra-coordinated iron(IV)-oxo.

The $[FeO(NH_3)_4]^{2+}$ complex is able to abstract a hydrogen from methane by two different pathways. The π-channel has a larger ΔE of 16.35 kcal mol^{-1} as apposed to the more favored σ-channel with a ΔE of 8.82 kcal mol^{-1}. The π-channel is available at smaller Fe-O-H angles and extended Fe-O bond distances. The σ-channel is available over a wider range of Fe-O-H distances, and the Fe-O bond length is typically shorter.

CASSCF/CASPT2 multireference calculations further elucidated the σ- and π-mechanisms of the TS. Upon analyzing the fractional orbital occupation numbers, it was clear that the σ- and π-mechanisms differed in electron arrangement. For the π-channel, an electron from one the the doubly degenerate (^{5}E) π orbitals to the singly degenerate σ^* orbital. Alternatively, the σ-channel occurs by an electron promotion from the singly degenerate (^{5}A) σ orbital to the σ^* orbital.

This study is in agreement with Vogiatzis and coworkers, which found that the π-mechanism is less accessible for psuedo trigonal bipyramidal iron(IV)-oxo complexes coordinated with NH_3 ligand, and that Fe-O bond lengths are directly associated with the oxyl radical character.[3] In the future, studies on a broader range of complexes with varying ligand fields will give a more comprehensive understanding of the σ- and π-mechanisms in Fe(IV)-oxo complexes.

3.5 Concluding Remarks

Electronic structure theory has proven a useful tool for elucidatinig mechanistic properties of small molecules. Working together with experimentalists and spectroscopists, computational chemistry promotes research advancements in the engineering of biomimetic catalysts. In Chapter 2, the binding modaility of the MoN_2 species was investigated for the purpose of nitrogen fixation. From this study and further studies on various dinitrogen-molybdenum complexes, the properties that contribute to the highly reactive MoFe-co active site in nitrogenase are elucidated. A selectively engineered catalysts influenced from studies like these will lead to a sustainable and low energy process. Chapter 3 focused on the study of an iron(IV)-oxo complex's role in the catalytic cycle of methane to methanol. We studied the most energy intensive step in the cycle, C-H activation. The σ- and π-channels in the $[FeO(NH_3)_4]^{2+}$ system were analyzed. The characteristics of the channel, angles, bond lengths, and MO diagrams, were elucidated through this study. With this information synthetic chemists can engineer a ligand environment suitable for methane activation. In the Vogiatzis research group, current studies in these topics are underway.[2 153 6]

Bibliography

[1] P. J. Dunn, "The importance of green chemistry in process research and development," 2012. iv

[2] P. Verma, K. D. Vogiatzis, N. Planas, J. Borycz, D. J. Xiao, J. R. Long, L. Gagliardi, and D. G. Truhlar, "Mechanism of oxidation of ethane to ethanol at Iron(IV)–oxo sites in magnesium-diluted Fe2(dobdc)," *Journal of the American Chemical Society*, vol. 137, no. 17, pp. 5770–5781, 2015. PMID: 25882096. iv, 47

[3] J. K. Kirkland, S. N. Khan, B. Casale, E. Miliordos, and K. D. Vogiatzis, "Ligand field effects on the ground and excited states of reactive FeO^{2+} species," *Phys. Chem. Chem. Phys.*, vol. 20, pp. 28786–28795, 2018. iv, ix, 30, 31, 33, 34, 35, 46

[4] B. M. Hoffman, D. Lukoyanov, Z.-Y. Yang, D. R. Dean, and L. C. Seefeldt, "Mechanism of nitrogen fixation by nitrogenase: The next stage," *Chemical Reviews*, vol. 114, no. 8, pp. 4041–4062, 2014. PMID: 24467365. viii, 16

[5] Y. Nishibayashi, "Development of catalytic nitrogen fixation using transition metal–dinitrogen complexes under mild reaction conditions," *Dalton Trans.*, vol. 47, pp. 11290–11297, 2018. viii, 17, 18, 19

[6] Y. Tanabe and Y. Nishibayashi, "Catalytic dinitrogen fixation to form ammonia at ambient reaction conditions using transition metal-dinitrogen complexes," *The Chemical Record*, vol. 16, no. 3, pp. 1549–1577, 2016. viii, 14, 17, 18, 19, 20, 29, 47

[7] P. L. Holland, "Metal-dioxygen and metal-dinitrogen complexes: where are the electrons?," *Dalton transactions (Cambridge, England : 2003)*, vol. 39, pp. 5415–5425, 06 2010. viii, 20, 21

[8] H. Schwarz, "Chemistry with methane: Concepts rather than recipes," *Angewandte Chemie International Edition*, vol. 50, no. 43, pp. 10096–10115, 2011. ix, 30, 31

[9] C. Krebs, D. Galonic Fujimori, C. T. Walsh, and J. M. Bollinger, "Non-heme Fe(IV)–oxo intermediates," *Accounts of Chemical Research*, vol. 40, no. 7, pp. 484–492, 2007. PMID: 17542550. ix, 32

[10] L. Que, "The road to non-heme oxoferryls and beyond," *Accounts of Chemical Research*, vol. 40, no. 7, pp. 493–500, 2007. PMID: 17595051. ix, 32, 33

[11] W. Nam, "High-valent Iron(IV)–Oxo complexes of heme and non-heme ligands in oxygenation reactions," *Accounts of Chemical Research*, vol. 40, no. 7, pp. 522–531, 2007. PMID: 17469792. ix, 32, 33

[12] D. Usharani, D. Janardanan, C. Li, and S. Shaik, "A theory for bioinorganic chemical reactivity of oxometal complexes and analogous oxidants: The exchange and orbital-selection rules," *Accounts of Chemical Research*, vol. 46, no. 2, pp. 471–482, 2013. PMID: 23210564. ix, 36

[13] N. S. O. Attila Szabo, *Modern Quantum Chemistry*. 1, 3, 4, 8

[14] F. Jensen, *Introduction to Computational Chemistry*. New York: John Wiley Sons, Incorporated, 2016. 2

[15] J. A. S. David Sholl, *Density Functional Theory: A Practical Approach*. 5, 6, 7, 8

[16] P. Hohenberg and W. Kohn, "Inhomogeneous electron gas," *Phys. Rev.*, vol. 136, pp. B864–B871, Nov 1964. 6

[17] R. M. D. Eberhard K. U. Gross, *Density Functional Theory*. 7

[18] J. Tirado-Rives and W. L. Jorgensen, "Performance of B3LYP density functional methods for a large set of organic molecules," *Journal of Chemical Theory and Computation*, vol. 4, no. 2, pp. 297–306, 2008. PMID: 26620661. 7

[19] T. Kato, "On the eigenfunctions of many-particle systems in quantum mechanics," *Communications on Pure and Applied Mathematics*, vol. 10, no. 2, pp. 151–177, 1957. 10

[20] E. R. Davidson and D. Feller, "Basis set selection for molecular calculations," *Chemical Reviews*, vol. 86, no. 4, pp. 681–696, 1986. 10

[21] B. O. Roos, *Multiconfigurational quantum chemistry for ground and excited states*, pp. 125–156. Dordrecht: Springer Netherlands, 2008. 12, 13

[22] T. H. P. J. J. Olsen, *Molecular Electronic Structure Theory*. 12

[23] J. W. Erisman, M. A. Sutton, J. Galloway, Z. Klimont, and W. Winiwarter, "How a century of ammonia synthesis changed the world," *Nature Geoscience*, vol. 1, pp. 636 EP –, 09 2008. 14, 17, 18

[24] D. Reay, *A Brief History of Nitrogen*, pp. 9–25. London: Palgrave Macmillan UK, 2015. 14

[25] *Catalysts for Nitrogen Fixation*. 14, 15

[26] M. C. Durrant, "Controlled protonation of iron-molybdenum cofactor by nitrogenase: a structural and theoretical analysis," *The Biochemical journal*, vol. 355, pp. 569–576, 05 2001. 14, 17

[27] M. C. Durrant, "An atomic-level mechanism for molybdenum nitrogenase. part 1. reduction of dinitrogen," *Biochemistry*, vol. 41, no. 47, pp. 13934–13945, 2002. PMID: 12437350. 14, 17

[28] Z. Cui, A. J. Dunford, M. C. Durrant, R. A. Henderson, and B. E. Smith, "Binding sites of nitrogenase: Kinetic and theoretical studies of cyanide binding to extracted FeMo-cofactor derivatives," *Inorganic Chemistry*, vol. 42, no. 20, pp. 6252–6264, 2003. PMID: 14514300. 14, 17

[29] M. C. Durrant, A. Francis, D. J. Lowe, W. E. Newton, and K. Fisher, "Evidence for a dynamic role for homocitrate during nitrogen fixation: the effect of substitution at the alpha-lys426 position in mofe-protein of azotobacter vinelandii," *The Biochemical journal*, vol. 397, pp. 261–270, 07 2006. 14, 17

[30] D. V. Yandulov and R. R. Schrock, "Catalytic reduction of dinitrogen to ammonia at a single molybdenum center," *Science*, vol. 301, no. 5629, pp. 76–78, 2003. 14, 19

[31] D. Tilman, K. G. Cassman, P. A. Matson, R. Naylor, and S. Polasky, "Agricultural sustainability and intensive production practices," *Nature*, vol. 418, pp. 671 EP –, 08 2002. 14

[32] A. G. Good and P. H. Beatty, "Fertilizing nature: A tragedy of excess in the commons," *PLOS Biology*, vol. 9, pp. 1–9, 08 2011. 15

[33] T. P. Hignett, *Ammonium Salts, Nitric Acid, and Nitrates*, pp. 83–108. Dordrecht: Springer Netherlands, 1985. 15

[34] J. Siegbahn, Per E. M. Westerberg, M. Svensson, and R. H. Crabtree, "Nitrogen fixation by nitrogenases: a quantum chemical study," *The Journal of Physical Chemistry B*, vol. 102, no. 9, pp. 1615–1623, 1998. 15

[35] C. Jodin 15

[36] "Studies in the biological fixation of nitrogen iii. the michaelis constant of nitrogenase in azotobacter vinelandii," *Biochimica et Biophysica Acta*, vol. 15, no. 3, pp. 390 – 394, 1954. 15

[37] D. Burk, H. Lineweaver, and C. K. Horner, "The specific influence of acidity on the mechanism of nitrogen fixation by azotobacter," *Journal of Bacteriology*, vol. 27, no. 4, pp. 325–340, 1934. 15

[38] W. Bulen, R. Burns, and J. LeComte, "Nitrogen fixation: Cell-free system with extracts of azotobacter," *Biochemical and Biophysical Research Communications*, vol. 17, no. 3, pp. 265 – 271, 1964. 15

[39] W. A. Bulen and J. R. LeComte, "The nitrogenase system from azotobacter: two-enzyme requirement for n2 reduction, ATP-dependent H2 evolution, and ATP hydrolysis," *Proceedings of the National Academy of Sciences of the United States of America*, vol. 56, pp. 979–986, 09 1966. 15

[40] K. C. Schneider, C. Bradbeer, R. N. Singh, L. C. Wang, P. W. Wilson, and R. H. Burris, "Nitrogen fixation by cell-free preparations from microorganisms," *Proceedings of the National Academy of Sciences of the United States of America*, vol. 46, pp. 726–733, 05 1960. 15

[41] B. K. Burgess, "The iron-molybdenum cofactor of nitrogenase," *Chemical Reviews*, vol. 90, no. 8, pp. 1377–1406, 1990. 15, 16

[42] J. B. Howard and D. C. Rees, "Structural basis of biological nitrogen fixation," *Chemical Reviews*, vol. 96, no. 7, pp. 2965–2982, 1996. PMID: 11848848. 15, 16

[43] H. C. Winter and R. H. Burris, "Nitrogenase," *Annual Review of Biochemistry*, vol. 45, no. 1, pp. 409–426, 1976. PMID: 183600. 15, 16

[44] B. K. Burgess and D. J. Lowe, "Mechanism of molybdenum nitrogenase," *Chemical Reviews*, vol. 96, no. 7, pp. 2983–3012, 1996. PMID: 11848849. 16

[45] W. J. BRILL and R. S. WOLFE, "Acetaldehyde oxidation by methanobacillus–a new ferredoxin-dependent reaction," *Nature*, vol. 212, no. 5059, pp. 253–255, 1966. 16

[46] W. Zumft and L. Mortenson, "The nitrogen-fixing complex of bacteria," *Biochimica et Biophysica Acta (BBA) - Reviews on Bioenergetics*, vol. 416, no. 1, pp. 1 – 52, 1975. 16

[47] R. V. Hageman and R. H. Burris, "Nitrogenase and nitrogenase reductase associate and dissociate with each catalytic cycle," *Proceedings of the National Academy of Sciences*, vol. 75, no. 6, pp. 2699–2702, 1978. 16

[48] D. R. Dean, J. T. Bolin, and L. Zheng, "Nitrogenase metalloclusters: structures, organization, and synthesis.," *Journal of Bacteriology*, vol. 175, no. 21, pp. 6737–6744, 1993. 16

[49] J. B. Howard and D. C. Rees, "Nitrogenase: A nucleotide-dependent molecular switch," *Annual Review of Biochemistry*, vol. 63, no. 1, pp. 235–264, 1994. PMID: 7979238. 16

[50] J. Kim and D. C. Rees, "Nitrogenase and biological nitrogen fixation," *Biochemistry*, vol. 33, no. 2, pp. 389–397, 1994. PMID: 8286368. 16

[51] V. K. Shah and W. J. Brill, "Isolation of an iron-molybdenum cofactor from nitrogenase," *Proceedings of the National Academy of Sciences of the United States of America*, vol. 74, pp. 3249–3253, 08 1977. 16

[52] J. W. Peters, K. Fisher, W. E. Newton, and D. R. Dean, "Involvement of the p cluster in intramolecular electron transfer within the nitrogenase MoFe protein," *Journal of Biological Chemistry*, vol. 270, no. 45, pp. 27007–27013, 1995. 16

[53] J. Kim and D. Rees, "Structural models for the metal centers in the nitrogenase molybdenum-iron protein," *Science*, vol. 257, no. 5077, pp. 1677–1682, 1992. 16

[54] L. Ma, M. A. Brosius, and B. K. Burgess, "Construction of a form of the mofe protein of nitrogenase that accepts electrons from the fe protein but does not reduce substrate," *Journal of Biological Chemistry*, vol. 271, no. 18, pp. 10528–10532, 1996. 16

[55] D. J. Lowe, K. Fisher, and R. N. F. Thorneley, "Klebsiella pneumoniae nitrogenase: pre-steady-state absorbance changes show that redox changes occur in the MoFe protein that depend on substrate and component protein ratio; a role for p-centres in reducing dinitrogen?," *Biochemical Journal*, vol. 292, no. 1, pp. 93–98, 1993. 16

[56] J. Kirn and D. C. Rees, "Crystallographic structure and functional implications of the nitrogenase molybdenum–iron protein from Azotobacter vinelandii," *Nature*, vol. 360, no. 6404, pp. 553–560, 1992. 16

[57] M. Chan, J. Kim, and D. Rees, "The nitrogenase FeMo-cofactor and p-cluster pair: 2.2 a resolution structures," *Science*, vol. 260, no. 5109, pp. 792–794, 1993. 16

[58] J. Kim, D. Woo, and D. C. Rees, "X-ray crystal structure of the nitrogenase molybdenum-iron protein from Clostridium pasteurianum at 3.0-.ANG. resolution," *Biochemistry*, vol. 32, no. 28, pp. 7104–7115, 1993. PMID: 8393705. 16

[59] R. R. Eady, "Structurefunction relationships of alternative nitrogenases," *Chemical Reviews*, vol. 96, no. 7, pp. 3013–3030, 1996. PMID: 11848850. 16

[60] S. B. Jang, L. C. Seefeldt, and J. W. Peters, "Insights into nucleotide signal transduction in nitrogenase: structure of an iron protein with mgadp bound,," *Biochemistry*, vol. 39, no. 48, pp. 14745–14752, 2000. PMID: 11101289. 16

[61] P. Strop, P. M. Takahara, H.-J. Chiu, H. C. Angove, B. K. Burgess, and D. C. Rees, "Crystal structure of the all-ferrous [4Fe-4S] ^{0} form of the nitrogenase iron protein from azotobacter vinelandii,," *Biochemistry*, vol. 40, no. 3, pp. 651–656, 2001. PMID: 11170381. 16

[62] S. B. Jang, L. C. Seefeldt, and J. W. Peters, "Modulating the midpoint potential of the [4Fe-4S] cluster of the nitrogenase Fe protein,,"

Biochemistry, vol. 39, no. 4, pp. 641–648, 2000. PMID: 10651628. 16

[63] T. Spatzal, M. Aksoyoglu, L. Zhang, S. L. A. Andrade, E. Schleicher, S. Weber, D. C. Rees, and O. Einsle, "Evidence for interstitial carbon in nitrogenase FeMo cofactor," *Science*, vol. 334, no. 6058, pp. 940–940, 2011. 17

[64] B. Hinnemann and J. K. N{o17
rskov, "Chemical activity of the nitrogenase femo cofactor with a central nitrogen ligand: Density functional study," *Journal of the American Chemical Society*, vol. 126, no. 12, pp. 3920–3927, 2004. PMID: 15038746.

[65] B. Hinnemann and J. K. Nørskov, "Structure of the fefe-cofactor of the iron-only nitrogenase and possible mechanism for dinitrogen reduction," *Phys. Chem. Chem. Phys.*, vol. 6, pp. 843–853, 2004. 17

[66] B. Hinnemann and J. K. Nørskov, "Catalysis by enzymes: The biological ammonia synthesis," *Topics in Catalysis*, vol. 37, pp. 55–70, Mar 2006. 17

[67] J. B. Varley, Y. Wang, K. Chan, F. Studt, and J. K. N{o17
rskov, "Mechanistic insights into nitrogen fixation by nitrogenase enzymes," *Phys. Chem. Chem. Phys.*, vol. 17, pp. 29541–29547, 2015.

[68] J. Kästner and P. E. Blöchl, "Ammonia production at the FeMo cofactor of nitrogenase: results from density functional theory," *Journal of the American Chemical Society*, vol. 129, no. 10, pp. 2998–3006, 2007. PMID: 17309262. 17

[69] V. Pelmenschikov, D. A. Case, and L. Noodleman, "Ligand-bound s = 1/2 femo-cofactor of nitrogenase: hyperfine interaction analysis and implication for the central ligand x identity," *Inorganic chemistry*, vol. 47, pp. 6162–6172, 07 2008. 17

[70] F. Neese, "The yandulov/schrock cycle and the nitrogenase reaction: Pathways of nitrogen fixation studied by density functional theory," *Angewandte Chemie International Edition*, vol. 45, no. 2, pp. 196–199, 2006. 17

[71] P. E. M. Siegbahn, "Model calculations suggest that the central carbon in the FeMo-cofactor of nitrogenase becomes protonated in the process of nitrogen fixation," *Journal of the American Chemical Society*, vol. 138, no. 33, pp. 10485–10495, 2016. PMID: 27454704. 17

[72] D. Rehder, "Vanadium nitrogenase," *Journal of Inorganic Biochemistry*, vol. 80, no. 1, pp. 133 – 136, 2000. 17

[73] D. C. Crans, J. J. Smee, E. Gaidamauskas, and L. Yang, "The chemistry and biochemistry of vanadium and the biological activities exerted by vanadium compounds," *Chemical Reviews*, vol. 104, no. 2, pp. 849–902, 2004. PMID: 14871144. 17

[74] K. Fisher, M. J. Dilworth, and W. E. Newton, "Azotobacter vinelandii vanadium nitrogenase: formaldehyde is a product of catalyzed hcn reduction, and excess ammonia arises directly from catalyzed azide reduction," *Biochemistry*, vol. 45, pp. 4190–4198, 04 2006. 17

[75] S. Duval, K. Danyal, S. Shaw, A. K. Lytle, D. R. Dean, B. M. Hoffman, E. Antony, and L. C. Seefeldt, "Electron transfer precedes atp hydrolysis during nitrogenase catalysis," *Proceedings of the National Academy of Sciences of the United States of America*, vol. 110, pp. 16414–16419, 10 2013. 17

[76] J. B. Howard and D. C. Rees, "How many metals does it take to fix N2? a mechanistic overview of biological nitrogen fixation," *Proceedings of the National Academy of Sciences*, vol. 103, no. 46, pp. 17088–17093, 2006. 17

[77] P. Wilson, A. Nyborg, and G. Watt, "Duplication and extension of the thorneley and lowe kinetic model for klebsiella pneumoniae nitrogenase catalysis using a mathematica software platform," *Biophysical Chemistry*, vol. 91, no. 3, pp. 281 – 304, 2001. 17

[78] M. G. Duyvis, H. Wassink, and H. Haaker, "Formation and characterization of a transition state complex of azotobacter vinelandii nitrogenase," *FEBS Letters*, vol. 380, no. 3, pp. 233 – 236, 1996. 17

[79] W. N. Lanzilotta, V. D. Parker, and L. C. Seefeldt, "Thermodynamics of nucleotide interactions with the azotobacter vinelandii nitrogenase iron protein," *Biochimica et Biophysica Acta (BBA) - Protein Structure and Molecular Enzymology*, vol. 1429, no. 2, pp. 411 – 421, 1999. 17

[80] L. E. Roth, J. C. Nguyen, and F. A. Tezcan, "ATP- and ironprotein-independent activation of nitrogenase catalysis by light," *Journal of the American Chemical Society*, vol. 132, no. 39, pp. 13672–13674, 2010. PMID: 20843032. 17

[81] F. Haber and G. Van Oordt, "Über die bildung von ammoniak aus den elementen," *Zeitschrift für anorganische Chemie*, vol. 47, no. 1, pp. 42–44, 1905. 17

[82] "Fritz haber – biographical." 17

[83] W. M. Stewart, D. W. Dibb, A. E. Johnston, and T. J. Smyth, "The contribution of commercial fertilizer nutrients to food production," vol. 97, pp. 1–6, 2005. 18

[84] "Nist standard reference simulation website,." 18, 25

[85] R. Lan, J. T. S. Irvine, and S. Tao, "Synthesis of ammonia directly from air and water at ambient temperature and pressure," *Scientific Reports*, vol. 3, pp. 1145 EP –, 01 2013. 18

[86] J. G. Chen, R. M. Crooks, L. C. Seefeldt, K. L. Bren, R. M. Bullock, M. Y. Darensbourg, P. L. Holland, B. Hoffman, M. J. Janik, A. K. Jones, M. G. Kanatzidis, P. King, K. M. Lancaster, S. V. Lymar, P. Pfromm, W. F. Schneider, and R. R. Schrock, "Beyond fossil fuel–driven nitrogen transformations," *Science*, vol. 360, no. 6391, 2018. 18

[87] "Fertilizers, climate change and enhancing agricultural productivity sustainability." 18

[88] U. N. E. Program, *Reactive nitrogen in the environment : too much or too little of a good thing*. 18

[89] J. N. Galloway, D. G. B. E. W. Dentener, F. J.and Capone, R. W. Howarth, S. P. Seitzinger, G. P. Asner, C. C. Cleveland, P. A. Green, E. A. Holland, D. M. Karl, A. F. Michaels, J. H. Porter, A. R. Townsend, and C. J. Vöosmarty, "Nitrogen cycles: Past, present, and future," *Biogeochemistry*, vol. 70, pp. 153–226, Sep 2004. 18

[90] F. Akagi, T. Matsuo, and H. Kawaguchi, "Dinitrogen cleavage by a diniobium tetrahydride complex: Formation of a nitride and its conversion into imide species," *Angewandte Chemie International Edition*, vol. 46, no. 46, pp. 8778–8781, 2007. 18

[91] H.-P. Jia and E. A. Quadrelli, "Mechanistic aspects of dinitrogen cleavage and hydrogenation to produce ammonia in catalysis and organometallic chemistry: relevance of metal hydride bonds and dihydrogen," *Chem. Soc. Rev.*, vol. 43, pp. 547–564, 2014. 18

[92] L. Manceron, O. Hübner, and H.-J. Himmel, "Dinitrogen activation by the Ti2N2 molecule: A matrix isolation study," *European Journal of Inorganic Chemistry*, vol. 2009, no. 5, pp. 595–598, 2009. 18

[93] L. P. Spencer, B. A. MacKay, B. O. Patrick, and M. D. Fryzuk, "Inner-sphere two-electron reduction leads to cleavage and functionalization of coordinated dinitrogen," *Proceedings of the National Academy of Sciences of the United States of America*, vol. 103, pp. 17094–17098, 11 2006. 18

[94] J. Chatt, A. J. Pearman, and R. L. Richards, "Conversion of dinitrogen in its molybdenum and tungsten complexes into ammonia and possible relevance to the nitrogenase reaction," *J. Chem. Soc., Dalton Trans.*, pp. 1852–1860, 1977. 19

[95] R. R. Schrock, "Catalytic reduction of dinitrogen to ammonia at a single molybdenum center," *Accounts of Chemical Research*, vol. 38, no. 12, pp. 955–962, 2005. PMID: 16359167. 19

[96] C. J. Cramer, M. Wloch, P. Piecuch, C. Puzzarini, and L. Gagliardi, "Theoretical models on the Cu2O2 torture track: mechanistic implications for oxytyrosinase and small-molecule analogues," *The Journal of Physical Chemistry A*, vol. 110, no. 5, pp. 1991–2004, 2006. PMID: 16451035. 20

[97] F. Aquilante, J. Autschbach, R. K. Carlson, L. F. Chibotaru, M. G. Delcey, L. De Vico, I. Fdez. Galván, N. Ferré, L. M. Frutos, L. Gagliardi, M. Garavelli, A. Giussani, C. E. Hoyer, G. Li Manni, H. Lischka, D. Ma, P. Malmqvist, T. Müller, A. Nenov, M. Olivucci, T. B. Pedersen, D. Peng, F. Plasser, B. Pritchard, M. Reiher, I. Rivalta, I. Schapiro, J. Segarra-Marti, M. Stenrup, D. G. Truhlar, L. Ungur, A. Valentini,

S. Vancoillie, V. Veryazov, V. P. Vysotskiy, O. Weingart, F. Zapata, and R. Lindh, "Molcas 8: New capabilities for multiconfigurational quantum chemical calculations across the periodic table," *Journal of Computational Chemistry*, vol. 37, no. 5, pp. 506–541, 2016. 21, 39

[98] J. Olsen, B. O. Roos, P. J{o21, 39
rgensen, and H. J. A. Jensen, "Determinant based configuration interaction algorithms for complete and restricted configuration interaction spaces," *The Journal of Chemical Physics*, vol. 89, no. 4, pp. 2185–2192, 1988.

[99] B. O. Roos, P. R. Taylor, and P. E. Siegbahn, "A complete active space SCF method (CASSCF) using a density matrix formulated super-CI approach," *Chemical Physics*, vol. 48, no. 2, pp. 157 – 173, 1980. 21, 39

[100] K. Andersson, P. Malmqvist, and B. O. Roos, "Second-order perturbation theory with a complete active space self-consistent field reference function," *The Journal of Chemical Physics*, vol. 96, no. 2, pp. 1218–1226, 1992. 21, 39

[101] B. O. Roos, R. Lindh, P. Malmqvist, V. Veryazov, and P. Widmark, "New relativistic ano basis sets for transition metal atoms," *The Journal of Physical Chemistry A*, vol. 109, no. 29, pp. 6575–6579, 2005. PMID: 16834004. 23, 39

[102] M. Reiher, "Douglas–kroll–hess theory: a relativistic electrons-only theory for chemistry," *Theoretical Chemistry Accounts*, vol. 116, no. 1, pp. 241–252, 2006. 23, 39

[103] B. A. Hess, "Relativistic electronic-structure calculations employing a two-component no-pair formalism with external-field projection operators," *Phys. Rev. A*, vol. 33, pp. 3742–3748, Jun 1986. 23, 39

[104] N. Forsberg and P. Åke Malmqvist, "Multiconfiguration perturbation theory with imaginary level shift," *Chemical Physics Letters*, vol. 274, no. 1, pp. 196 – 204, 1997. 23, 39

[105] "A modified definition of the zeroth-order hamiltonian in multiconfigurational perturbation theory (CASPT2)," *Chemical Physics Letters*, vol. 396, no. 1, pp. 142 – 149, 2004. 23, 39

[106] D. Schröder and H. Schwarz, "C-H and C-C bond activation by bare transition-metal oxide cations in the gas phase," *Angewandte Chemie International Edition in English*, vol. 34, no. 18, pp. 1973–1995, 1995. 30

[107] T. Z. H. Gani and H. J. Kulik, "Understanding and breaking scaling relations in single-site catalysis: Methane to methanol conversion by Fe(IV)O," *ACS Catalysis*, vol. 8, no. 2, pp. 975–986, 2018. 30

[108] P. D. G. A. Olah, D. A. Goeppert, and P. D. G. K. S. Prakash, *Beyond Oil and Gas: The Methanol Economy, Second Edition*. 31

[109] D. Schröder, A. Fiedler, J. Hrusak, and H. Schwarz, "Experimental and theoretical studies toward a characterization of conceivable intermediates involved in the gas-phase oxidation of methane by bare FeO+. generation of four distinguishable [Fe,C,H4,O]+ isomers," *Journal of the American Chemical Society*, vol. 114, no. 4, pp. 1215–1222, 1992. 31

[110] M. F. Ryan, A. Fiedler, D. Schröder, and H. Schwarz, "Radical-like behavior of manganese oxide cation in its gas-phase reactions with dihydrogen and alkanes," *Journal of the American Chemical Society*, vol. 117, no. 7, pp. 2033–2040, 1995. 31

[111] Y. Shiota and K. Yoshizawa, "Methane-to-methanol conversion by first-row transition-metal oxide ions: ScO+, TiO+, VO+, CrO+, MnO+, FeO+, CoO+, NiO+, and CuO+," *Journal of the American Chemical Society*, vol. 122, no. 49, pp. 12317–12326, 2000. 31

[112] D. Schröder and H. Schwarz, "Gas-phase activation of methane by ligated transition-metal cations," *Proceedings of the National Academy of Sciences*, vol. 105, no. 47, pp. 18114–18119, 2008. 31

[113] J. X. Wang and J. H. Lunsford, "Characterization of [Li+O] centers in lithium-doped magnesium oxide catalysts," *The Journal of Physical Chemistry*, vol. 90, no. 22, pp. 5883–5887, 1986. 31

[114] C. E. Tinberg and S. J. Lippard, "Dioxygen activation in soluble methane monooxygenase," *Accounts of Chemical Research*, vol. 44, no. 4, pp. 280–288, 2011. PMID: 21391602. 32

[115] R. P. Hausinger, "Fe(II)/ {alpha32 -ketoglutarate-dependent hydroxylases and related enzymes," *Critical Reviews in Biochemistry and Molecular Biology*, vol. 39, no. 1, pp. 21–68, 2004.

[116] J. E. Baldwin and M. Bradley, "Isopenicillin N synthase: mechanistic studies," *Chemical Reviews*, vol. 90, no. 7, pp. 1079–1088, 1990. 32

[117] M. L. Neidig, A. Decker, O. W. Choroba, F. Huang, M. Kavana, G. R. Moran, J. B. Spencer, and E. I. Solomon, "Spectroscopic and electronic structure studies of aromatic electrophilic attack and hydrogen-atom abstraction by non-heme iron enzymes," *Proceedings of the National Academy of Sciences*, vol. 103, no. 35, pp. 12966–12973, 2006. 32

[118] B. E. Eser, E. W. Barr, P. A. Frantom, L. Saleh, J. M. Bollinger, C. Krebs, and P. F. Fitzpatrick, "Direct spectroscopic evidence for a high-spin Fe(IV) intermediate in tyrosine hydroxylase," *Journal of the American Chemical Society*, vol. 129, no. 37, pp. 11334–11335, 2007. PMID: 17715926. 32

[119] P. Gandeepan, T. Müller, D. Zell, G. Cera, S. Warratz, and L. Ackermann, "3d transition metals for C–H activation," *Chemical Reviews*, vol. 119, no. 4, pp. 2192–2452, 2019. 32

[120] "High-valent nonheme iron-oxo species in biomimetic oxidations," *Journal of Inorganic Biochemistry*, vol. 100, no. 4, pp. 421 – 433, 2006. High-valent iron intermediates in biology. 32

[121] K. Hashimoto, S. Nagatomo, S. Fujinami, H. Furutachi, S. Ogo, M. Suzuki, A. Uehara, Y. Maeda, Y. Watanabe, and T. Kitagawa, "A new mononuclear Iron(III) complex containing a peroxocarbonate ligand," *Angewandte Chemie International Edition*, vol. 41, no. 7, pp. 1202–1205, 2002. 32

[122] W. N. Oloo and L. Que, "Bioinspired nonheme iron catalysts for C–H and C-C bond oxidation: Insights into the nature of the metal-based oxidants," *Accounts of Chemical Research*, vol. 48, no. 9, pp. 2612–2621, 2015. PMID: 26280131. 32

[123] T. J. Collins, "Designing ligands for oxidizing complexes," *Accounts of Chemical Research*, vol. 27, no. 9, pp. 279–285, 1994. 32

[124] T. J. Collins, K. L. Kostka, E. Munck, and E. S. Uffelman, "Stabilization of mononuclear five-coordinate iron(iv)," *Journal of the American Chemical Society*, vol. 112, no. 14, pp. 5637–5639, 1990. 32

[125] V. Sobolev, K. Dubkov, O. Panna, and G. Panov, "Selective oxidation of methane to methanol on a FeZSM-5 surface," *Catalysis Today*, vol. 24, no. 3, pp. 251 – 252, 1995. Proceedings of the Second Workshop on C1-C3 Hydrocarbon Conversion. 33

[126] K. Dubkov, N. Ovanesyan, A. Shteinman, E. Starokon, and G. Panov, "Evolution of iron states and formation of {alpha33 -sites upon activation of FeZSM-5 zeolites," *Journal of Catalysis*, vol. 207, no. 2, pp. 341 – 352, 2002.

[127] B. E. R. Snyder, P. Vanelderen, M. L. Bols, S. D. Hallaert, L. H. Böttger, L. Ungur, K. Pierloot, R. A. Schoonheydt, B. F. Sels, and E. I. Solomon, "The active site of low-temperature methane hydroxylation in iron-containing zeolites," *Nature*, vol. 536, pp. 317 EP –, 08 2016. 33

[128] D. J. Xiao, E. D. Bloch, J. A. Mason, W. L. Queen, M. R. Hudson, N. Planas, J. Borycz, A. L. Dzubak, P. Verma, K. Lee, F. Bonino, V. Crocella, J. Yano, S. Bordiga, D. G. Truhlar, L. Gagliardi, C. M. Brown, and J. R. Long, "Oxidation of ethane to ethanol by N2O in a metal–organic framework with coordinatively unsaturated iron(II) sites," *Nature Chemistry*, vol. 6, pp. 590 EP –, 05 2014. 33

[129] P. Liao, R. B. Getman, and R. Q. Snurr, "Optimizing open iron sites in metal–organic frameworks for ethane oxidation: A first-principles study," *ACS Applied Materials & Interfaces*, vol. 9, no. 39, pp. 33484–33492, 2017. PMID: 28394564. 33

[130] P. Verma, K. D. Vogiatzis, N. Planas, J. Borycz, D. J. Xiao, J. R. Long, L. Gagliardi, and D. G. Truhlar, "Mechanism of oxidation of ethane to ethanol at Iron(IV)–Oxo sites in magnesium-diluted Fe2(dobdc)," *Journal of the American Chemical Society*, vol. 137,

no. 17, pp. 5770–5781, 2015. PMID: 25882096. 33

[131] H. Hirao, W. K. H. Ng, A. M. P. Moeljadi, and S. Bureekaew, "Multiscale model for a metal–organic framework: High-spin rebound mechanism in the reaction of the Oxoiron(IV) species of Fe-MOF-74," *ACS Catalysis*, vol. 5, no. 6, pp. 3287–3291, 2015. 33

[132] A. Bassan, M. R. Blomberg, T. Borowski, and P. E. Siegbahn, "Theoretical studies of enzyme mechanisms involving high-valent iron intermediates," *Journal of Inorganic Biochemistry*, vol. 100, no. 4, pp. 727 – 743, 2006. High-valent iron intermediates in biology. 33

[133] L. Que, "The road to non-heme oxoferryls and beyond," *Accounts of Chemical Research*, vol. 40, no. 7, pp. 493–500, 2007. PMID: 17595051. 33

[134] J. England, M. Martinho, E. Farquhar, J. R. Frisch, E. Bominaar, E. Münck, and L. Que Jr., "A synthetic high-spin Oxoiron(IV) complex: Generation, spectroscopic characterization, and reactivity," *Angewandte Chemie International Edition*, vol. 48, no. 20, pp. 3622–3626, 2009. 33

[135] E. A. Hill, A. C. Weitz, E. Onderko, A. Romero-Rivera, Y. Guo, M. Swart, E. L. Bominaar, M. T. Green, M. P. Hendrich, D. C. Lacy, and A. S. Borovik, "Reactivity of an fe(IV)-oxo complex with protons and oxidants," *Journal of the American Chemical Society*, vol. 138, pp. 13143–13146, 10 2016. 33

[136] J. P. Bigi, W. H. Harman, B. Lassalle-Kaiser, D. M. Robles, T. A. Stich, J. Yano, R. D. Britt, and C. J. Chang, "A high-spin iron(IV)–oxo complex supported by a trigonal nonheme pyrrolide platform," *Journal of the American Chemical Society*, vol. 134, no. 3, pp. 1536–1542, 2012. PMID: 22214221. 33

[137] D. Schröder, S. Shaik, and H. Schwarz, "Two-state reactivity as a new concept in organometallic chemistry," *Accounts of Chemical Research*, vol. 33, no. 3, pp. 139–145, 2000. PMID: 10727203. 33

[138] S. Shaik, H. Chen, and D. Janardanan, "Exchange-enhanced reactivity in bond activation by metal–oxo enzymes and synthetic reagents," *Nature Chemistry*, vol. 3, pp. 19 EP –, 12 2010. 33

[139] S. Meyer, I. Klawitter, S. Demeshko, E. Bill, and F. Meyer, "A tetracarbene–oxoiron(IV) complex," *Angewandte Chemie International Edition*, vol. 52, no. 3, pp. 901–905, 2013. 33

[140] R. Kumar, A. Ansari, and G. Rajaraman, "Axial vs. equatorial ligand rivalry in controlling the reactivity of iron(IV)-oxo species: Single-state vs. two-state reactivity," *Chemistry – A European Journal*, vol. 24, no. 26, pp. 6818–6827, 2018. 33

[141] C. Kupper, B. Mondal, J. Serrano-Plana, I. Klawitter, F. Neese, M. Costas, S. Ye, and F. Meyer, "Nonclassical single-state reactivity of an oxo-iron(IV) complex confined to triplet pathways," *Journal of the American Chemical Society*, vol. 139, no. 26, pp. 8939–8949, 2017. PMID: 28557448. 33, 34, 37

[142] M. Srnec, S. D. Wong, J. England, L. Que, and E. I. Solomon, "π-frontier molecular orbitals in S={ 34
2 ferryl species and elucidation of their contributions to reactivity," *Proceedings of the National Academy of Sciences*, vol. 109, no. 36, pp. 14326–14331, 2012.

[143] E. I. Solomon, K. M. Light, L. V. Liu, M. Srnec, and S. D. Wong, "Geometric and electronic structure contributions to function in non-heme iron enzymes," *Accounts of Chemical Research*, vol. 46, no. 11, pp. 2725–2739, 2013. PMID: 24070107. 34

[144] E. Andris, R. Navratil, J. Jasik, T. Terencio, M. Srnec, M. Costas, and J. Roithova, "Chasing the evasive FeO stretch and the spin state of the Iron(IV)–Oxo complexes by photodissociation spectroscopy," *Journal of the American Chemical Society*, vol. 139, no. 7, pp. 2757–2765, 2017. PMID: 28125220. 34

[145] M. Srnec, S. D. Wong, M. L. Matthews, C. Krebs, J. M. Bollinger, and E. I. Solomon, "Electronic structure of the ferryl intermediate in the {alpha34, 36
-ketoglutarate dependent non-heme iron halogenase SyrB2: Contributions to h atom abstraction reactivity," *Journal of the American Chemical Society*, vol. 138, no. 15, pp. 5110–5122, 2016. PMID: 27021969.

[146] C. B. Bell III, S. D. Wong, Y. Xiao, E. J. Klinker, A. L. Tenderholt, M. C. Smith, J.-U. Rohde, L. Que Jr., S. P. Cramer, and E. I. Solomon, "A combined NRVS and DFT study of FeIV-O model complexes: A diagnostic method for the elucidation of non-heme iron enzyme intermediates," *Angewandte Chemie International Edition*, vol. 47, no. 47, pp. 9071–9074, 2008. 34

[147] M. Srnec, S. D. Wong, and E. I. Solomon, "Excited state potential energy surfaces and their interactions in FeIV-O active sites," *Dalton Trans*, vol. 43, pp. 17567–17577, 2014. 34

[148] S. Ye and F. Neese, "Nonheme oxo-iron(IV) intermediates form an oxyl radical upon approaching the c-h bond activation transition state," *Proceedings of the National Academy of Sciences*, vol. 108, no. 4, pp. 1228–1233, 2011. 34

[149] B. K. Mai and Y. Kim, "Is it Fe(iii)-oxyl radical that abstracts hydrogen in the C–H activation of TauD? a theoretical study based on the DFT potential energy surfaces," *Inorganic Chemistry*, vol. 55, no. 8, pp. 3844–3852, 2016. PMID: 27031914. 34

[150] H. Chen, W. Lai, and S. Shaik, "Exchange-enhanced H-abstraction reactivity of high-valent nonheme Iron(IV)-oxo from coupled cluster and density functional theories," *The Journal of Physical Chemistry Letters*, vol. 1, no. 10, pp. 1533–1540, 2010. 36

[151] S. D. Wong, M. Srnec, M. L. Matthews, L. V. Liu, Y. Kwak, K. Park, C. B. Bell III, E. E. Alp, J. Zhao, Y. Yoda, S. Kitao, M. Seto, C. Krebs, J. M. Bollinger, and E. I. Solomon, "Elucidation of the Fe(IV)=o intermediate in the catalytic cycle of the halogenase SyrB2," *Nature*, vol. 499, pp. 320 EP –, 07 2013. 36

[152] D. Fang, R. L. Lord, and G. A. Cisneros, "*Ab Initio* QM/MM calculations show an intersystem crossing in the hydrogen abstraction step in dealkylation catalyzed by AlkB," *The Journal of Physical Chemistry B*, vol. 117, no. 21, pp. 6410–6420, 2013. PMID: 23642148. 37

[153] P. C. Andrikopoulos, C. Michel, S. Chouzier, and P. Sautet, "*In Silico* screening of Iron-Oxo catalysts for CH bond cleavage," *ACS Catalysis*, vol. 5, no. 4, pp. 2490–2499, 2015. 37, 47

[154] "TURBOMOLE V6.6 2014, a development of University of Karlsruhe and Forschungszentrum Karlsruhe GmbH, 1989-2007, TURBOMOLE GmbH, since 2007; available from `http://www.turbomole.com`.." 37, 38

[155] A. D. Becke, "Density-functional thermochemistry. III. the role of exact exchange," *The Journal of Chemical Physics*, vol. 98, no. 7, pp. 5648–5652, 1993. 37

[156] F. Weigend and R. Ahlrichs, "Balanced basis sets of split valence, triple zeta valence and quadruple zeta valence quality for h to rn: Design and assessment of accuracy," *Phys. Chem. Chem. Phys.*, vol. 7, pp. 3297–3305, 2005. 37, 38

[157] F. Weigend, "Accurate coulomb-fitting basis sets for h to rn," *Phys. Chem. Chem. Phys.*, vol. 8, pp. 1057–1065, 2006. 37, 38

[158] E. Torres and G. A. DiLabio, "A (nearly) universally applicable method for modeling noncovalent interactions using B3LYP," *The Journal of Physical Chemistry Letters*, vol. 3, no. 13, pp. 1738–1744, 2012. PMID: 26291852. 38

[159] S. Grimme, S. Ehrlich, and L. Goerigk, "Effect of the damping function in dispersion corrected density functional theory," *Journal of computational chemistry*, vol. 32 7, pp. 1456–65, 2011. 38

[160] X. Ren, P. Rinke, V. Blum, J. Wieferink, A. Tkatchenko, A. Sanfilippo, K. Reuter, and M. Scheffler, "Resolution-of-identity approach to hartree–fock, hybrid density functionals, RPA, MP2 andGWwith numeric atom-centered orbital basis functions," *New Journal of Physics*, vol. 14, p. 053020, may 2012. 38

[161] F. Weigend, "Hartree–fock exchange fitting basis sets for H to Rn," *Journal of Computational Chemistry*, vol. 29, no. 2, pp. 167–175, 2008. 38

[162] H. B. Schlegel, "Optimization of equilibrium geometries and transition structures," *Journal of Computational Chemistry*, vol. 3, no. 2, pp. 214–218, 1982. 38

[163] O. Treutler and R. Ahlrichs, "Efficient molecular numerical integration schemes," *The Journal of Chemical Physics*, vol. 102, no. 1, pp. 346–354, 1995. 38

[164] "Chemcraft - graphical software for visualization of quantum chemistry computations." 41